scientific reports

Check for updates

OPEN

Effect of cubebin against streptozotocin-induced diabetic nephropathy rats via inhibition TNF-α/NF-κB/TGF-β: in vivo and in silico study

Rahamat Unissa Syed[1]✉, Sivakumar S. Moni[2,9]✉, Weiam Hussein[3], Taghreed Mohammad Saad Alhaidan[4], Sondos Mohammed Y. Abumilha[5], Lama Khalid Alnahdi[5], Ling Shing Wong[6], Vetriselvan Subramaniyan[7] & Vinoth Kumarasamy[8]✉

Cubebin, a dibenzyl butyrolactone lignan belonging to several distinct families, including *Aristolochiaceae*, *Myristicaceae*, *Piperaceae*, and *Rutaceae*, and possesses several pharmacological activities, including analgesic, anti-inflammatory, antioxidant, and vasodilatory. The current study aimed to evaluate the effect of cubebin on streptozotocin (STZ)-evoked diabetic nephropathy (DN). DN is a well-identified complication of diabetes mellitus (DM) characterized by renal hypertrophy that progressively declines kidney function. Wistar rats were randomly divided into groups- normal, STZ control (65 mg/kg/body weight), and STZ + cubebin (10 and 20 mg/kg). Biochemical parameters such as glucose levels, kidney parameters, lipid profile, oxidative stress, endogenous antioxidant markers, inflammatory cytokines and histopathology were performed. Molecular docking [(PDB ID: TNF-α (7JRA), NF-κB (1SVC), TGF-β1 (3TZM)] and dynamic simulation (MDS) were also performed with the selected target. STZ-induced DN was changes in these parameters. In contrast, DN + cubebin at 10 and 20 mg/kg doses improved the biochemical parameters and histological changes. Furthermore, molecular docking and simulation studies showed a binding affinity with negative binding energy with TNF-α (7jra, − 11.342 kcal/mol), TGF-β1 (3tzm, − 9.162 kcal/mol) and NF-κB (1svc, − 6.665 kcal/mol). The results of MDS provided insight into the mechanisms that associate proteins TNF-α, NF-κB, and TGF-β1 in conformational dynamics upon binding to cubebin. In conclusion, these findings exhibit a potential effect of cubebin in STZ-evoked DN rats.

Keywords Antioxidant, Cubebin, Diabetic nephropathy, Streptozotocin, Diabetes

Diabetes mellitus (DM) is an endocrine disorder associated with abnormal metabolism of carbohydrates, protein, and lipids[1,2], elevating blood glucose levels[3]. This elevated blood glucose level occurs due to abnormal pancreatic β cells and results in abnormal insulin production[4]. Diabetes type 1 and type 2 both involve abnormal insulin action, including insulin resistance and insulin sensitivity[5,6]. The macrovascular and microvascular complications are well-established risk factors for DM. These complications are distinguished by distinct

[1]Department of Pharmaceutics, College of Pharmacy, University of Ha'il, Ha'il 81442, Saudi Arabia. [2]Department of Pharmaceutics, College of Pharmacy, Jazan University, Jazan 45142, Saudi Arabia. [3]Department of Pharmaceutical Chemistry, College of Pharmacy, University of Hail, Hail 81442, Saudi Arabia. [4]Department of Clinical Toxicology, College of Medicine, Umm Al-Qura University, Mecca, Saudi Arabia. [5]College of Medicine, King Khalid University, Abha, Saudi Arabia. [6]Faculty of Health and Life Sciences, INTI International University, Nilai 71800, Malaysia. [7]Division of Pharmacology, School of Medical and Life Sciences, Sunway University, No. 5, Jalan Universiti, Bandar Sunway, 47500 Selangor Darul Ehsan, Kuala Lumpur 47500, Malaysia. [8]Department of Parasitology and Medical Entomology, Faculty of Medicine, Universiti Kebangsaan Malaysia, Jalan Yaacob Latif, Cheras, Kuala Lumpur 56000, Malaysia. [9] Health Research Center, Jazan University, Jazan 45142, Saudi Arabia. ✉email: ru.syed@outlook.com; ru.syed@uoh.edu.sa; smoni@jazanu.edu.sa; vinoth.ukm@hotmail.com

pathological features, including diabetic nephropathy (DN), neuropathy, cardiovascular disease, and retinopathy. DN, also known as diabetic kidney disease, emerges as a prevalent complication within the DM population, affecting approximately 30–40% of patients and manifesting as diabetic renal disease[7,8]. DN constitutes a prevalent microvascular complication of DM affecting the kidneys. It is characterized by renal hypertrophy, a decline in renal function, and renal fibrosis accompanied by the accumulation of extracellular matrices and a decreased glomerular filtration rate, leading to kidney failure[9–11]. DN development is influenced by a confluence of risk factors, including dyslipidemia, hypertension, suboptimal glycemic control, and smoking[12]. Additionally, a person's genetic predisposition plays a crucial role, as indicated by the elevated susceptibility of individuals with a familial history of DN[11]. Unfortunately, the aetiology and pathogenesis of DN remain elusive. DN arises in a complex multifactorial way, including the generation of advanced glycation end products (AGEs), growth factor elaboration (VEGF, angiopoietins), and hemodynamic/hormonal alterations. These lead to activating reactive oxygen species (ROS) and inflammatory mediators[13]. The unrestrained ROS trigger a state of oxidative stress, further promoting the secretion of pro-inflammatory cytokines, particularly nuclear factor-kappa B (NF-κB), interleukin-6 (IL-6), interleukin-1beta (IL-1β), and tumour necrosis factor-alpha (TNF-α)[14,15]. These inflammatory mediators are significant in the DN, followed by glomerular hyperfiltration, hypertension, hypertrophy, and altered composition, leading to albuminuria and hypertension[16]. Another factor, such as sugar-derived AGEs, accumulates in the kidney due to impaired renal clearance, potentially worsening DN. VEGF activation and angiopoietin-driven proliferation promote vascular changes, potentially contributing to DN[17,18].

Pathologically, the kidney undergoes various alterations and exhibits mesangial matrix expansion, thickening of the glomerular basement membrane, cellular proliferation, and tubular atrophy, culminating in interstitial fibrosis and glomerulosclerosis, the hallmark of chronic kidney disease[19].

Streptozotocin (STZ), a broad-spectrum antibiotic derived from the *bacterium Streptomyces achromogenes*, exhibits diabetogenic properties. These chemically N-nitrosourea-containing glucosan derivatives act as an alkylating antineoplastic agent with selective toxicity towards pancreatic β-cells in mammals[20,21]. Following this intervention, the animals develop a constellation of symptoms, including insulin deficiency (insulinopenia), elevated blood glucose (hyperglycemia), excessive thirst (polydipsia), and increased urination (polyuria). These manifestations are indicative of DM in humans, and notably, STZ administration is utilized to induce a type 1 DM state in experimental animal models[22].

The current therapy for DN within clinical practice focuses on early intervention. Meticulous glycemic control via antihyperglycemic agents alongside renin-angiotensin system blockade using ACE inhibitors or ARBs demonstrably mitigates DN progression to overt nephropathy[23]. These medications remain the mainstay treatment for DN. However, plant-derived phytochemicals have the potential to be preventative agents for DN[24]. Each herb contains a diverse array of phytochemicals, with only a select few exhibiting demonstrably anti-diabetic effects[25,26]. Cubebin, a derivative of dibenzyl butyrolactone lignan, has been identified and extracted from various plant species belonging to several distinct families, including *Aristolochiaceae*, *Myristicaceae*, *Rutaceae*, and *Piperaceae*.

It exhibits several pharmacological activities, including trypanocidal, antimycobacterial, analgesic, anti-inflammatory, and vasodilatory[27]. The present investigation was designed to assess cubebin in vivo antidiabetic potential in STZ-evoked diabetic rats and in silico the selectivity of TNF-α, NF-Kβ, and TGF-β1 via molecular docking and molecular dynamic simulation (MDS). The investigation aimed to assess any subsequent alterations in biochemical and haematological parameters.

Materials and methods

Animals

Wistar rats (180 ± 20 g, 8-10-week-old male) were procured and acclimated for ten days before the commencement of the study. The rats were housed at a controlled temperature (22 ± 3 °C) and a relative humidity of 55 ± 5%. A 12-hour light/dark cycle was maintained. Standard laboratory chow and purified water were given ad libitum. The Institutional Animal Ethical Committee, following ARRIVE guidelines, approved the experiment.

Drugs and chemicals

STZ was acquired from Sigma Aldrich, USA. Cubebin ($C_{20}H_{20}O_6$, MW- 356.37, purity ≥ 98.0%) was obtained from MSW Pharma, M.S., India. Biochemical kits were used to determine insulin and proinflammatory cytokines from MSW Pharma, M.S., India. Serum lipid Profile and kidney function test were determined using a commercially available kit from Lupin Diagnostic, M.S., India.

Acute toxicity studies and prediction of ADMET by computational analysis

The cubebin doses for this investigation were selected based on previously published studies in Wistar rats. These studies demonstrated that oral administration of cubebin at doses ranging from 10 to 20 mg/kg body weight[28–30]. A rapid assessment of cubebin's pharmacokinetic and toxicity properties was performed using pkCSM ADMET descriptors[31].

Experimental design

Induction of DN

Type 1 DM was induced overnight fasted rats and then given STZ (65 mg/kg body weight) intraperitoneal injection[32]. STZ was freshly prepared in a 10 mM citrate buffer solution with a pH of 4.5. Three days after STZ administration, hyperglycemia was assessed using a tail vein blood sample with a OneTouch Glucometer (Accu-Check Active, Roche Diagnostics, India). Rats with blood glucose levels consistently above 250 mg/dL for three consecutive days were considered DM. These DM rats were maintained on standard rat chow and tap water ad libitum for four weeks. At the end of this period, all DM rats were housed in individual metal metabolic cages

for the precise collection of 24-hour urine samples. A urinary albumin excretion rate exceeding 30 mg/24 hours was recorded at week 4, confirming the successful establishment of DN[33].

Experimental protocol
The DN model preparation was described above, the rats were allocated to four groups, each having six rats (Fig. 1). Group I served as normal rats (0.5 ml of normal saline). Group II comprised STZ-injected T1DM control rats. Groups III and IV-STZ + 10 and 20 mg/kg body weight (BW) of cubebin were administered orally[28,29]. Treatment of cubebin was started on day 3 after STZ injection, in the morning time each day, and lasted for week 8. Blood glucose concentrations and body weight were assessed at regular intervals.

Biochemical parameters

Biological sample preparations
At the end of the experiments, urine samples were collected from rats housed in metabolic cages. The rats were euthanized by administering ketamine /xylazine (75/10 mg/kg/ i.p.) at the end of the experiment. Blood was withdrawn and kept at − 80 °C until used for biochemical parameters. The collected blood underwent centrifugation at 1000 rpm for 15–20 min to isolate serum. The kidney was isolated after scarification of animals by using cervical dislocation. Kidneys were excised from each rat. Subsequently, the isolated kidney was dissected into smaller pieces and frozen at − 80 °C for biochemical assays.

Estimation of glucose and serum insulin
Following a 6-hour fasting, blood was collected through a tail-prick approach, utilizing a commercially available glucometer to determine blood glucose level. A small quantity of each sample was then applied to a glucometer test strip for subsequent blood glucose determination (Accu chek strips, Roche-Diabetes Care). Baseline blood glucose concentrations were established before the initiation of the experiment, with follow-up measurements taken upon experiment completion (At 1, 4, and 8 weeks). The concentration of serum insulin (µIU/ml) was determined by utilizing an ELISA.

Estimation of hemoglobin A1c (HbA1c)
Hemoglobin A1c (HbA1c) concentration was measured using an ELISA kit from MSW Pharma, M.S., India. The estimation of HbA1c was examined using the manufacturer's instructions.

Determination of serum lipid profile
Whole blood samples underwent centrifugation at room temperature for 10 min to isolate serum. Following centrifugation, the isolated serum was stored below − 50 °C. Determination of TC, TG, and HDL-C was carried out utilizing commercially available biochemical kits Lupin Diagnostic, M.S., India.

Estimation of kidney function test
Using commonly available diagnostic kits from Lupin Diagnostic, M.S., India, the serum and urine samples were analyzed spectrophotometrically to quantify creatinine (Scr) and blood urea nitrogen (BUN) levels. Absorbance measurements were performed at 254 nm for serum and 340 nm for urine. Urine volume was also measured.

Estimation of biomarkers of oxidative stress
The antioxidant enzymes, including superoxide dismutase-SOD, catalase-CAT, glutathione reductase-GSH, and malondialdehyde-MDA, were performed in kidney homogenate using a commercially available diagnostic ELISA kit from MSW Pharma, M.S., India.

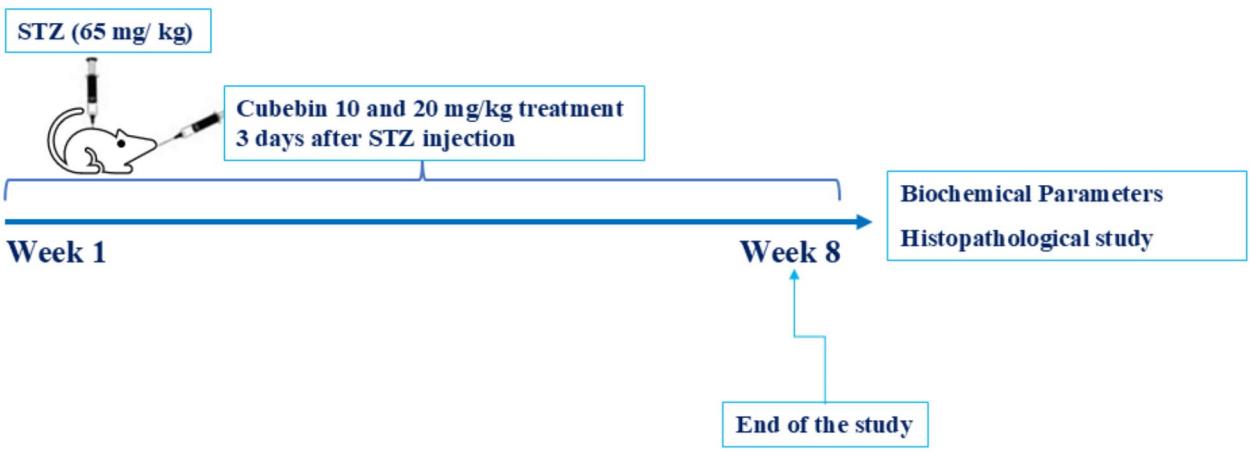

Fig. 1. Experimental design.

Determination of proinflammatory cytokines
Diagnostic ELISA kits determined pro-inflammatory cytokines in kidney homogenate including TNF-α (MSW-TNF-α), IL-1β (MSW-IL-1β), and IL-6 (MSW-IL-6).

Determination of NF-κB and TGF-β1
Commercially diagnostic ELISA kits were used for the determination of the NF-κB (MSW-NF-κB) and TGF-β1 (MSW-TGF-β1) in kidney homogenate.

Histopathology
Renal tissues were excised and immediately immersed in a 10% formalin-phosphate buffered solution for fixation. Subsequently, tissues were embedded in paraffin wax within metal cassettes and refrigerated for solidification. Paraffin-embedded tissues were sectioned at 3–5 µm thickness using a microtome to generate cross-sections. Hematoxylin and eosin (H&E) staining was performed on these sections to assess renal histological architecture. Two independent, blinded investigators evaluated the stained sections under light microscopy.

Molecular docking studies

Target protein retrieval and preparation
RCSB Protein Data Bank provides the crystal structure of TNF-α (PDB ID: 7JRA), NF-κβ (PDB ID: 1SVC), and TGF-β1 (PDB ID: 3TZM). Several factors, including the wwPDB validation report, resolution, mutation rate, the existence of a co-crystallized ligand, and Ramachandran plot, were used to validate the isolated structures. Table 1 compares the standard values and the retrieved protein to validate the chosen protein for the docking study. In this study, protein structures were optimized and minimized using the software package CHIMERA v1.16. To account for the energetic interactions of both standard and non-standard residues, AMBER ff14SB and AM1-BCC force fields were employed, respectively. Subsequently, all non-standard residues, including water molecules, co-crystal ligands, and redundant protein chains, were eliminated from the structures.

Grid generation
Docking simulations were facilitated by AutoDock Tools (version 1.5.65) and Chimera (version 1.112) for grid generation and validation. The grid parameters were established based on the co-crystal ligand orientation whenever available. Alternatively, the CASTp6 server was employed for apo-state proteins to determine favourable ligand binding pockets. The dimensions of the docking box were minimized to ensure optimal alignment of geometry and character with the active site of protein to accommodate the anticipated ligand structures.

Ligands preparation
The ligand cubebin was retrieved from the ChemSpider database and prepared for computational analysis using Marvin Sketch software. The 2D and 3D structures were optimized to eliminate any inconsistencies or errors. The resulting structures were then subjected to energy minimization using the MMFF94 force field to identify the most stable conformation. This lowest energy conformer was selected for further investigation and exported in the MOL2 file format for compatibility with computational chemistry software.

Molecular docking of the target protein with ligands

After retrieving, the protein and ligand structure were prepared for docking simulations. In-house scripts, utilizing AutoDock Tools 1.5.6 for ADFRsuit for proteins and ligands, were employed to convert the structures into the pdbqt file format. These scripts ensured complete rotational freedom for all ligand torsions while treating the receptor as a rigid molecule. AutoDock Vina 1.2.3 was subsequently used for docking calculations, with a grid spacing of 0.375 Å (Table 2).

The docking simulation was centred on the active site of targets using a well-defined grid box. This approach facilitated exploring the program of potential ligand-receptor interactions beyond the immediate active site cavity. Standard parameters were employed for all other aspects of the simulation. The XYZ defined the grid box dimensions coordinates provided in Table 3. Additional parameters included CPU cores set to 23, exhaustiveness set to 32, number of generated binding poses set to 9, and energy range set to 3 kcal/mol. Redocking simulations were performed using the identical configuration parameters in the initial docking runs.

Parameters	Details			Standards
Target	TNF-α	NF-Kβ	TGF-β1	
Protein Id	7JRA	1SVC	3TZM	–
Method of experiment	X-ray diffraction	X-ray diffraction	X-ray diffraction	X-ray diffraction
Mutation	No	No	No	No
Resolution	2.10Å	2.60Å	1.70Å	Near about 3.00 Å
wwPDB Validation	Better	Better	Better	Better
Co-Crystal Ligand	VGY	Absent	085	–
Ramchandran Plot (by PROCHECK server) Residues in favoured + Allowed regions	99.1%	97%	99.5%	> 88%

Table 1. Comparison of retrieved protein with standard values validation of selected protein for docking study.

Protein ID	The active sites amino acids
7JRA	LEU133A, TYR135A, VAL199A, ILE231A, ALA232A, LEU233A, LEU133B, TYR135B, TYR195B, GLY197B, GLY198B, LEU133C, TYR135C, SER136C, LEU196C, GLY197C, TYR227C, ILE231C
1SVC	LYS52P, ARG54P, GLY55P, SER243P, ALA248P, SER249P, ASN250P, LEU251P, ARG336P, GLU341P, THR342P, SER343P, GLU344P
3TZM	ILE211A, GLY214A, ARG215A, ALA230A, LYS232A, LEU260A, LEU278A, SER280A, ASP281A, TYR282A, HIS283A, LYS335A, LYS337A, ASN338A, LEU340A, ASP351A

Table 2. The active sites amino acids.

Sr.no	Protein Id	Centre coordinates			Size coordinates		
		x	y	z	x	y	z
1	7JRA	− 14.33	− 2.46	− 26.34	25	25	25
2	1SVC	34.401	9.319	37.650	20	20	20
3	3TZM	4.53	8.72	6.78	25	25	25

Table 3. Grid parameter.

Sr. no.	Name of compound	Binding energy (kcal/mol)	Type of interaction	Residue ID	Distance Å
1	7jra_Cubebin	− 11.342	Hydrophobic interactions	LEU133A	3.1
				LEU133B	3.53
				LEU133C	3.92
				LEU133C	3.59
				TYR135C	3.46
				TYR135C	3.51
				TYR135C	3.29
				TYR195B	3.73
				LEU233A	3.64
			Hydrogen Bonds	SER136C	2.76
				LEU196C	2.49
				LEU196C	1.88
2	1svc_Cubebin	− 6.665	Hydrogen bonds	GLN53P	2.16
				LEU251P	2.28
				LEU251P	2.99
				THR342P	2.87
			π-cation interactions	LYS52P	4.98
3	3tzm_Cubebin	− 9.162	Hydrophobic interactions	VAL219A	3.62
				VAL219A	3.39
				ALA230A	3.36
				LEU260A	3.98
				LEU340A	3.65
				LEU340A	3.56
			Hydrogen bonds	LYS232A	2.35
				SER280A	2.03
				SER287A	2.11
				SER287A	2.67
				ASP290A	2.13

Table 4. Docking score and intermolecular interactions of ligands with protein TNF-α (PDB ID 7JRA), NF-Kβ (PDB ID 1SVC), TGF-β1 (PDB ID 3TZM) PLIP.

Visualization

Following docking simulations with AutoDock Vina, the resultant ligand-receptor complexes were visualized and analyzed utilizing the Biovia Discovery Studio visualizer. Subsequently, two-dimensional (2D) and three-dimensional (3D) images of the complex structure were generated using Maestro 12.3 (academic edition) (Table 4).

MDS

MD simulations were conducted on protein-ligand complexes for PDB IDs 1SVC, 3TZM, and 7JRA bound to cubebin ligand using Desmond v2020.1 (Schrödinger, LLC). The OPLS-2005 force field[34–36] and an explicit solvent model with TIP3P water molecules[37] were employed. The simulations were conducted within a periodic boundary box with dimensions of 10 Å × 10 Å × 10 Å. Na + ions were added at a concentration of 0.15 M to maintain system neutrality, mimicking a physiological NaCl solution. Initial system equilibration was achieved utilizing an NVT ensemble for 10 ns, allowing the protein-ligand complexes to adapt to the simulated environment.

Following equilibration and minimization, a brief (12 ns) NPT ensemble simulation was performed to ensure system equilibration at the target conditions. The Nose-Hoover thermostat with a relaxation time of 1.0 ps was employed to retain a constant temperature throughout the simulation. The Martyna-Tuckerman–Klein barostat, with a relaxation time of 2 ps, was utilized to control targeting a pressure of 1 bar. A time step of 2 femtoseconds (fs) was used for the simulation[38]. The interaction between long-range electrostatic was evaluated using the particle mesh Ewald method[39] with a Coulomb potential cutoff radius of 9 Å. A RESPA integrator with a timestep of 2 femtoseconds (fs) per short step was employed to integrate the bonded interactions for each simulated trajectory.

The principal component analysis investigated the conformational space explored during the MD simulations. The geometric parameters incorporated cumulative factors such as radius of gyration, values of eigen, and Sham variables that enable the visualization in a 3D plot generated using the Matplotlib Python library[40]. The simulation of MD was carried out for 100 ns. The MDS stability was assessed with the use of root mean square deviation (RMSD), root mean square fluctuation (RMSF), and radius of gyration (Rg), along with the computation of hydrogen bonds, bridges of salt, and solvent-accessible surface area (SASA)[41].

Binding free energy analysis

The ΔG_{bind} of ligand-protein complexes was identified using the generalized born surface area (MM-GBSA) technique. Remarkably, the principle MM-GBSA ΔG_{bind} was combined for 50 frames of the simulation trajectory by the sampling stride of one frame and employment of Python script.

An additive interaction model was utilized to determine MM-GBSA ΔG_{bind} (kcal/mol). This model degrades the total free energy into contributions from individual energy terms such as Coulombic, H-bond, covalent, van der Waals, lipophilic, self-contact, and solvation components for ligand and protein (Table 5).

ΔG_{bind} is calculated using the following:

$$\Delta G_{bind} = \Delta G_{MM} + \Delta G_{Solv} - \Delta G_{SA}$$

where, ΔGbind represents the binding free energy, ΔGMM represents the difference between the free energies of ligand-protein complexes and the total energies of the isolated form of protein-ligand, ΔGSolv represents the difference in the GSA solvation energies of the ligand-receptor complex and the sum of the solvation energies of the receptor and the ligand in the unbound state, ΔGSA represents the difference in surface area energy for the interaction of protein and ligand.

Statistical analysis

GraphPad Prism software was utilized to analyse experimental data as mean ± SEM. The numerical variation of the result data was assessed using the Shapiro-Wilk test. A one-way analysis of variance (ANOVA) was employed to compare means between groups ($n = 6$ animals/group). Following a significant ANOVA result ($P < 0.05$), Tukey's multiple comparison tests were utilized for post hoc analysis to detect specific group differences.

Results

Acute toxicity assessment

The selection of a 10 and 20 mg/kg dosage of cubebin for the present study did not elicit any observable signs of toxicity or cause mortality, indicating a favorable safety profile within this dosage range. The predicted oral rat acute toxicity of cubebin LD50 was 2.5 mol/kg. The pharmacokinetics and toxicity predictions of cubebin are presented in Table 6.

Energies (kcal/mol)	1SVC_Cubebin	3TZM_Cubebin	7JRA_Cubebin
ΔG_{bind}	− 50.10 ± 3.22	− 52.84 ± 1.57	− 47.75 ± 3.45
$\Delta G_{bindCoulomb}$	− 15.90 ± 1.43	− 10.14 ± 2.87	− 9.42 ± 3.31
$\Delta G_{bindCovalent}$	2.14 ± 0.76	1.99 ± 0.99	1.70 ± 0.90
$\Delta G_{bindHbond}$	− 1.39 ± 0.30	− 0.94 ± 0.25	− 0.64 ± 0.46
$\Delta G_{bind\ Lipo}$	− 13.04 ± 0.91	− 22.11 ± 1.83	− 26.16 ± 2.36
$\Delta G_{bindSolvGB}$	23.65 ± 1.32	20.29 ± 1.33	36.27 ± 5.87
$\Delta G_{bindvdW}$	− 44.78 ± 2.94	− 41.86 ± 2.28	− 49.51 ± 2.66

Table 5. The components of ΔG_{bind} for the 1SVC_Cubebin calculated by MM-GBSA.

Property	Model name	predicted value	Unit
Absorption	Water solubility	− 4.516	Numeric (log mol/L)
	Caco2 (human colon adenocarcinoma cells) permeability	1.236	Numeric (log Papp in 10^{-6} cm/s)
	Intestinal absorption (human)	97.749	Numeric (% Absorbed)
	Skin Permeability	− 2.865	Numeric (log Kp)
	P-glycoprotein substrate	Yes	Categorical (Yes/No)
	P-glycoprotein I inhibitor	Yes	Categorical (Yes/No)
	P-glycoprotein II inhibitor	No	Categorical (Yes/No)
Distribution	BBB permeability	− 1.111	Numeric (log BB)
	CNS permeability	− 3.08	Numeric (log PS)
Metabolism	CYP2D6 substrate	No	Categorical (Yes/No)
	CYP3A4 substrate	Yes	Categorical (Yes/No)
	CYP1A2 inhibitior	No	Categorical (Yes/No)
	CYP2C19 inhibitior	Yes	Categorical (Yes/No)
	CYP2C9 inhibitior	No	Categorical (Yes/No)
	CYP2D6 inhibitior	No	Categorical (Yes/No)
	CYP3A4 inhibitior	Yes	Categorical (Yes/No)
Excretion	Total Clearance	− 0.117	Numeric (log ml/min/kg)
	Renal OCT2 substrate	No	Categorical (Yes/No)
Toxicity	Oral Rat Acute Toxicity (LD50)	2.5	Numeric (mol/kg)
	Oral Rat Chronic Toxicity (LOAEL)	1.584	Numeric (log mg/kg_bw/day)
	Hepatotoxicity	No	Categorical (Yes/No)
	Skin Sensitisation	No	Categorical (Yes/No)

Table 6. Pharmacokinetics and toxicity predict of cubebin. *BBB* blood-brain barrier, *CNS* central nervous system, *CYP* cytochrome, *LD50* lethal dose 50, *OCT2* organic cation transporter 2.

Body weight

The body weight was decreased in the STZ-induced DN rats but increased in the normal group ($P < 0.01$). At the end of the study (8 weeks after administration of STZ), no significant difference was detected between the DN and the cubebin in both dose groups ($P > 0.05$), represented in Fig. 2A.

Glucose and insulin level

Figure 2B-C demonstrates the outcome of cubebin on the FBG and insulin on STZ-induced DN rats. STZ-evoked DN rats exhibited a marked elevation in FBG and a concomitant decrease in serum insulin concentration compared to control rats, which confirms the progression of a diabetic state in the STZ-evoked DN rats ($P < 0.01$). The administration of cubebin at both doses demonstrated an appreciable reduction [$F(3, 20) = 64.82$, ($P < 0.0001$)] in the FBG level and restored the level of insulin [$F(3, 20) = 14.45$, $P < 0.0001$]. This finding demonstrated the potential effect of cubebin against STZ-induced DN rats.

HbA1c

As shown in Fig. 3, HbA1c was altered during DN. STZ-evoked DN rats demonstrated an elevated level of HbA1c as associated with normal group rats ($P < 0.01$). However, cubebin administration facilitates the level of HbA1c% [$F(3, 20) = 12.10$, $P < 0.0001$] as associated with the STZ-evoked DN group.

Serum lipid profile

DN is associated with significant dyslipidemia, as evidenced by elevated concentrations of TC and TG in the DN group associated with the control group ($P < 0.01$). Conversely, HDL-C levels were markedly reduced ($P < 0.01$) in the DN rats (Fig. 4A–C). However, cubebin treatment reduced significantly the level of TC [$F(3, 20) = 79.80$, $P < 0.0001$], TG [$F(3, 20) = 65.32$, $P < 0.0001$], and elevated the level of HDL [$F(3, 20) = 18.30$, $P < 0.0001$]. Notably, the ameliorating effects of cubebin at both doses of 10 and 20 mg/kg on serum lipid profile in DN rats.

Kidney function test

The effect of cubebin on STZ-induced renal dysfunction and established biomarkers of DN were evaluated in Fig. 5A-C. Scr and BUN concentrations in the diabetic control group exhibited a statistically significant ($P < 0.01$) increase associated with the normal group, signifying characteristic hallmarks of DN. However, after administration of cubebin (10 and 20 mg/kg), the kidney injury biomarkers were decreased in Scr [$F(3, 20) = 6.882$, $P = 0.0023$] and BUN [$F(3, 20) = 11.07$, $P = 0.0002$] and urine volume [$F(3, 20) = 38.75$, $P < 0.0001$] in association with the DN rats. Notably, cubebin effectively ameliorates renal dysfunction in STZ-evoked DN rats.

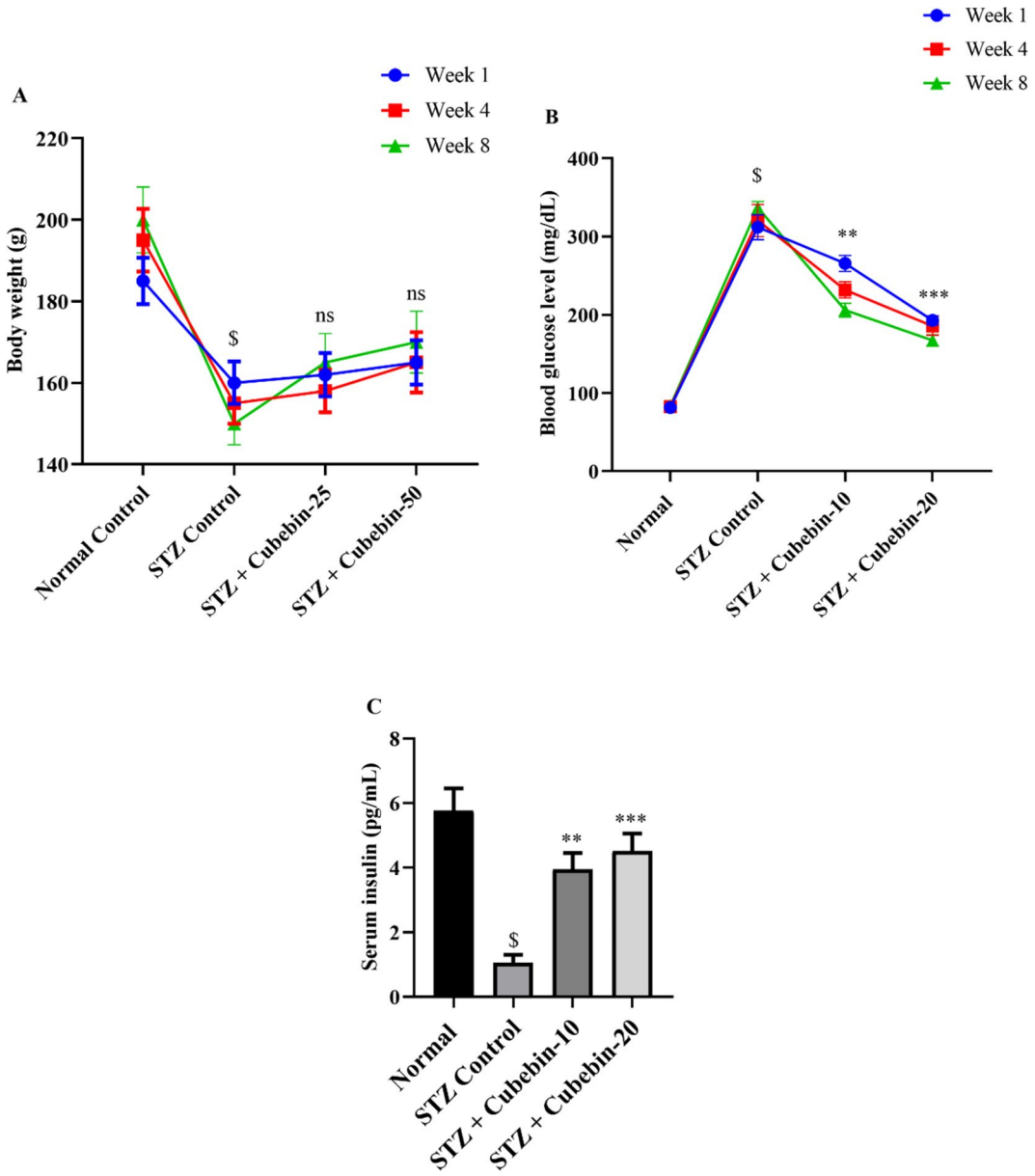

Fig. 2. (**A–C**) Cubebin effect on (**A**) body weight (**B**) blood glucose level and (**C**) serum insulin level (**, ***, $P < 0.001$, $P < 0.0001$, *ns* not significant; Tukey's test).

Biomarkers of oxidative stress and endogenous antioxidants

The potential modulatory effect of cubebin on oxidative enzymes and oxidative stress markers. Rats induced with STZ exhibited a marked reduction in SOD, GSH, and CAT, while elevation in MDA was associated with the DN group rats ($P < 0.01$). As illustrated in Fig. 6A–D, DN rats treated with cubebin reduced the level of GSH F (3, 20) = 15.85, $P < 0.0001$], SOD [F (3, 20) = 13.29, $P < 0.0001$], GSH, and CAT [F (3, 20) = 16.19, $P < 0.0001$] in serum, but significantly elevated MDA [F (3, 20) = 10.91, $P = 0.0002$]. However, cubebin administration ameliorates oxidative stress and endogenous antioxidants in the DN rats.

Proinflammatory cytokines

The result shown in Fig. 7A–C suggests a significant alteration in the profile of pro-inflammatory cytokines during the development of STZ-evoked DN that exhibited elevated levels of TNF-α, IL-1β, and IL-6 associated with normal rats ($P < 0.01$). Cubebin administration restored the level of TNF-α [F (3, 20) = 42.24, $P < 0.0001$], IL-1β [F (3, 20) = 38.91, $P < 0.0001$], and IL-6 [F (3, 20) = 41.15, $P < 0.0001$] as associated to STZ-evoked DN rats.

Determination of NF-κB and TGF-β1

Figure 8A,B demonstrates the outcome of NF-κB and TGF-β1 on the different rat groups. STZ-evoked DN rats demonstrated marked elevation of NF-κB and TGF-β1 as associated with treated and normal rats ($P < 0.01$).

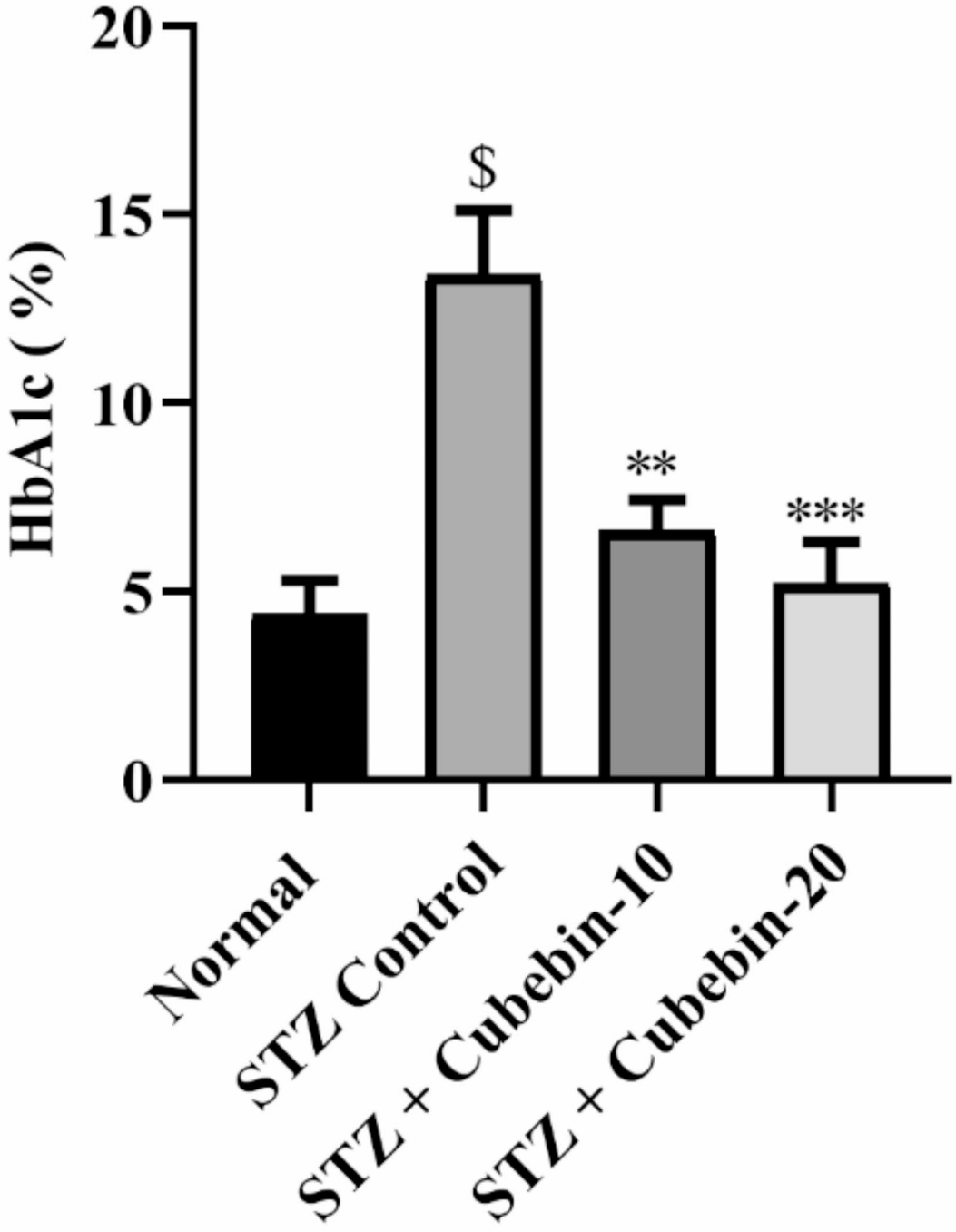

Fig. 3. Cubebin effect on HbA1c (**, ***, $P < 0.001$, $P < 0.0001$; Tukey's test).

Treatment with cubebin markedly reduced the level of NF-Kb [F (3, 20) = 37.50, $P < 0.0001$] and TGF-β1 [F (3, 20) = 53.07, $P < 0.0001$].

Histology

Diabetic control rats displayed healthy renal tissue with normal glomeruli and tubules. In contrast, diabetic rats induced by STZ exhibited significant renal damage, characterized by glomerular basement membrane thickening, cellular necrosis, interstitial inflammation, hemorrhage, and severe glomerular injury. Importantly,

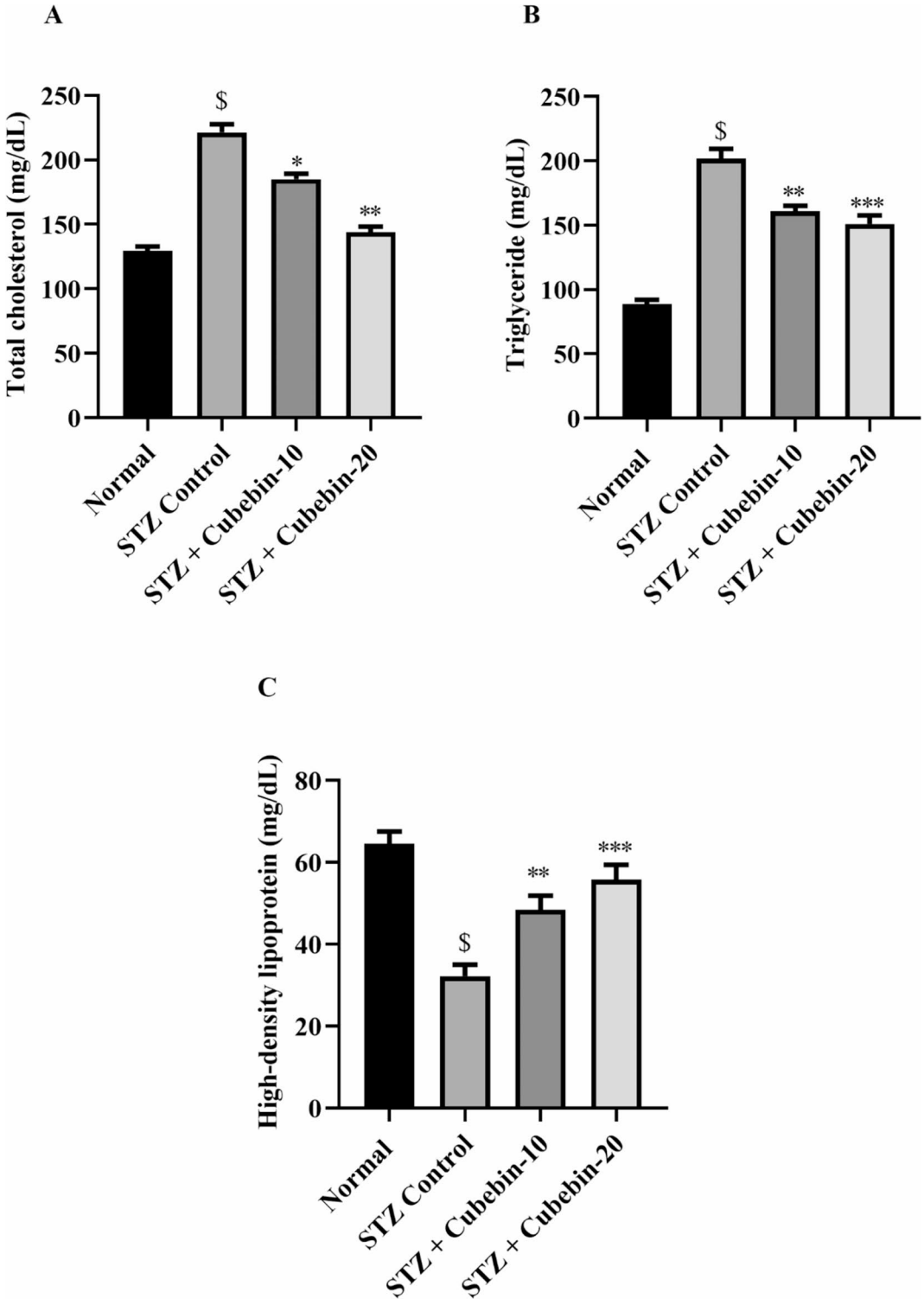

Fig. 4. (**A–C**) Cubebin effect on serum lipid profile (**A**) total cholesterol. (**B**) Triglyceride. (**C**) High-density lipoprotein (*, **, ***, $P < 0.05$, $P < 0.001$, $P < 0.0001$; Tukey's test).

treatment with cubebin at both low and high doses resulted in a marked improvement in renal morphology, with restoration of normal glomerular and tubular structures. These findings indicate that cubebin effectively mitigates renal pathology in DN rats by attenuating the majority of observed lesions. The histological changes in STZ-induced DN are illustrated in Fig. 9A–D.

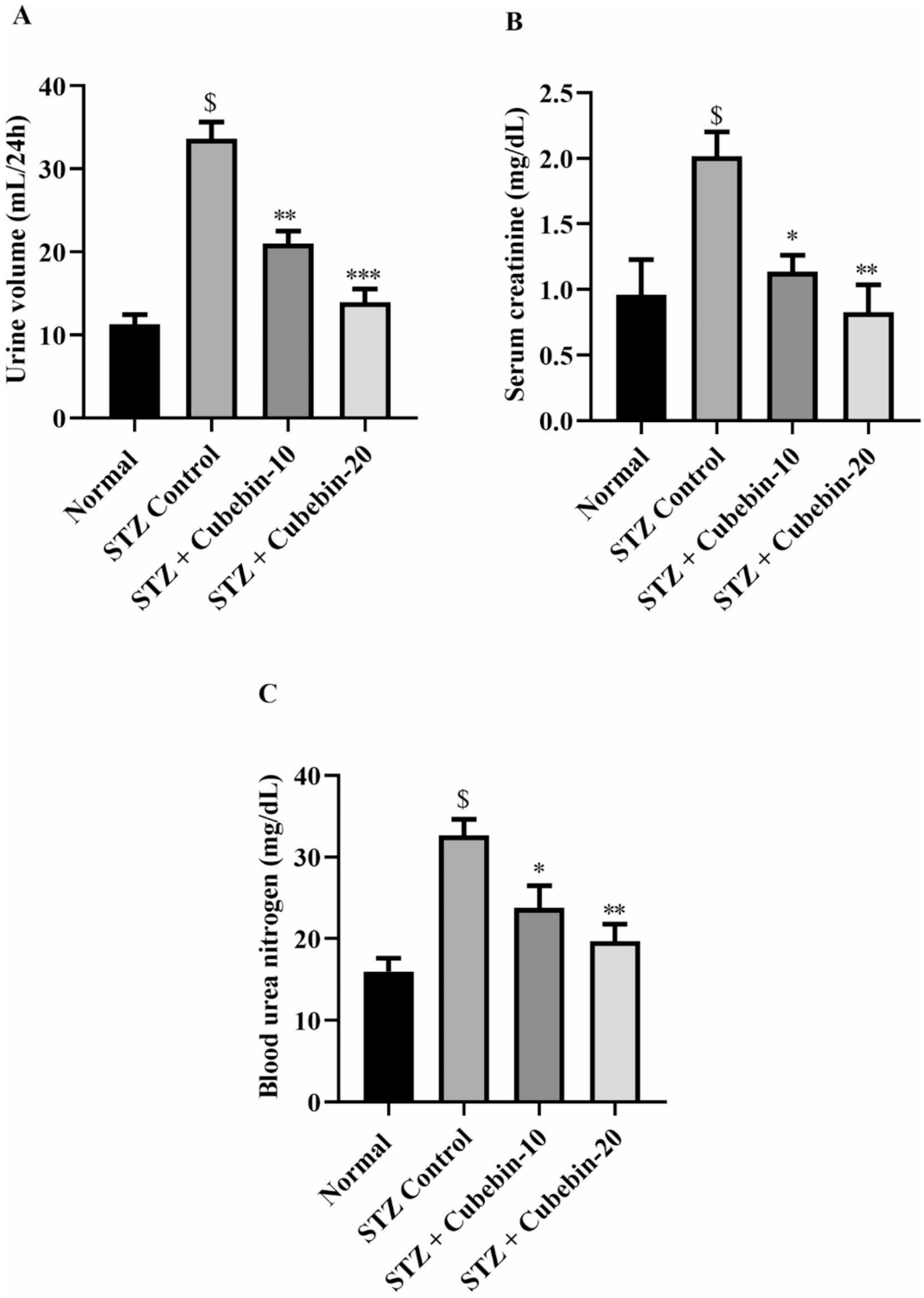

Fig. 5. (**A**–**C**) Cubebin effect on Kidney function test (**A**) Urine volume (**B**) Serum creatinine (**C**) Blood urea nitrogen (*, **, ***, $P < 0.05$, $P < 0.001$, $P < 0.0001$; Tukey's test).

Molecular docking

Docking analysis revealed favourable binding interactions between cubebin and target proteins (PDB ID: 7JRA, 1SVC, 3TZM) with respective binding affinities of -11.342, -6.665, and −9.162 kcal/mol (Table 4). Cubebin exhibited the strongest affinity towards 7JRA (− 11.342 kcal/mol) among these. The interaction profile suggests the involvement of hydrogen and hydrophobic bonds between Cubebin and TNF-α, NF-Kβ, and TGF-β1. These interactions may potentially obstruct conserved and functionally critical residues within the active sites of the target proteins (7JRA, 1SVC, 3TZM). Collectively, the docking results proposed that cubebin treatment might

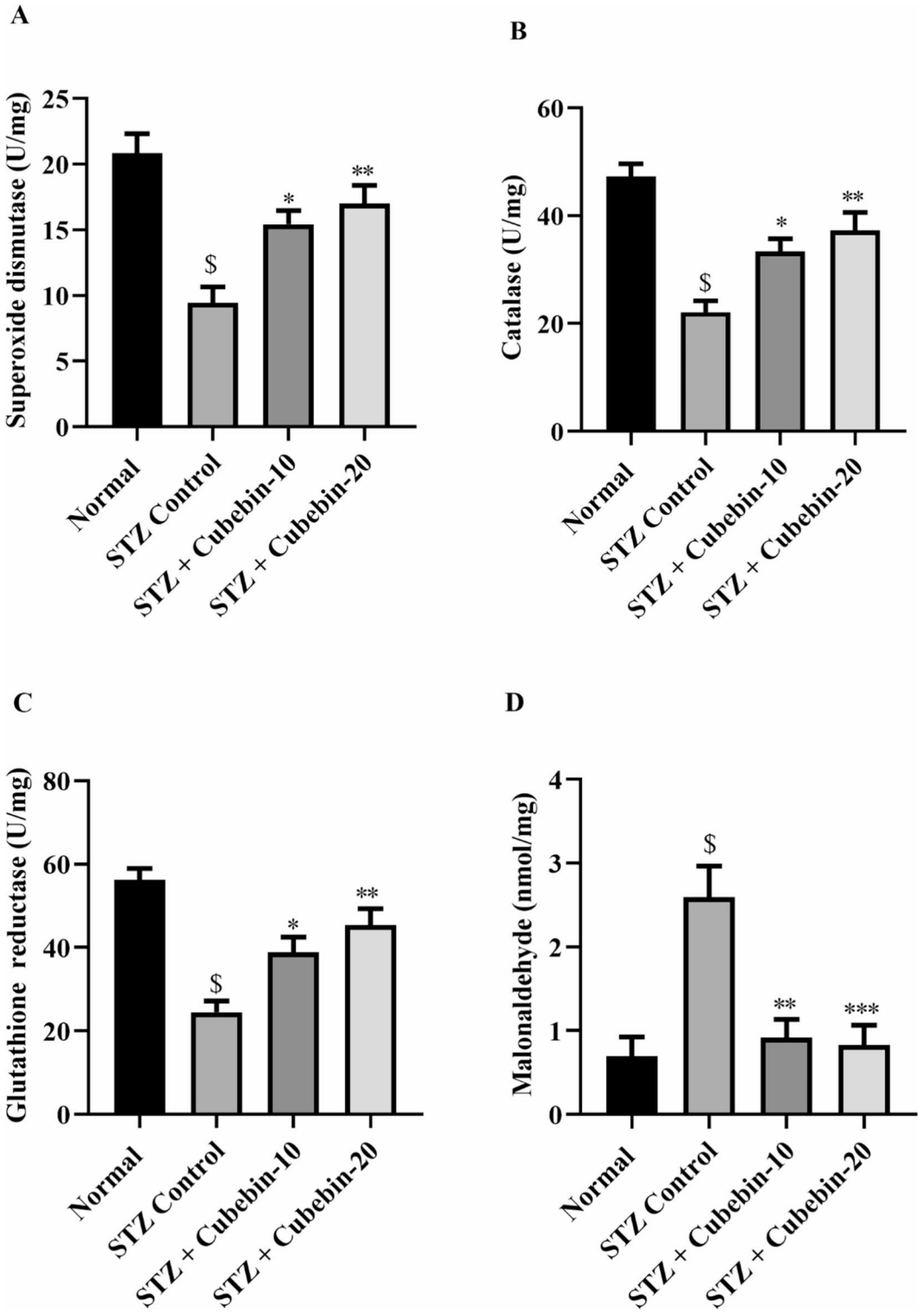

Fig. 6. (**A**–**D**) Cubebin effect on oxidative stress biomarker (**A**) Superoxidase, (**B**) Catalase (**C**) Glutathione, (**D**) Malonaldehyde (*, **, ***, $P < 0.05$, $P < 0.001$, $P < 0.0001$; Tukey's test).

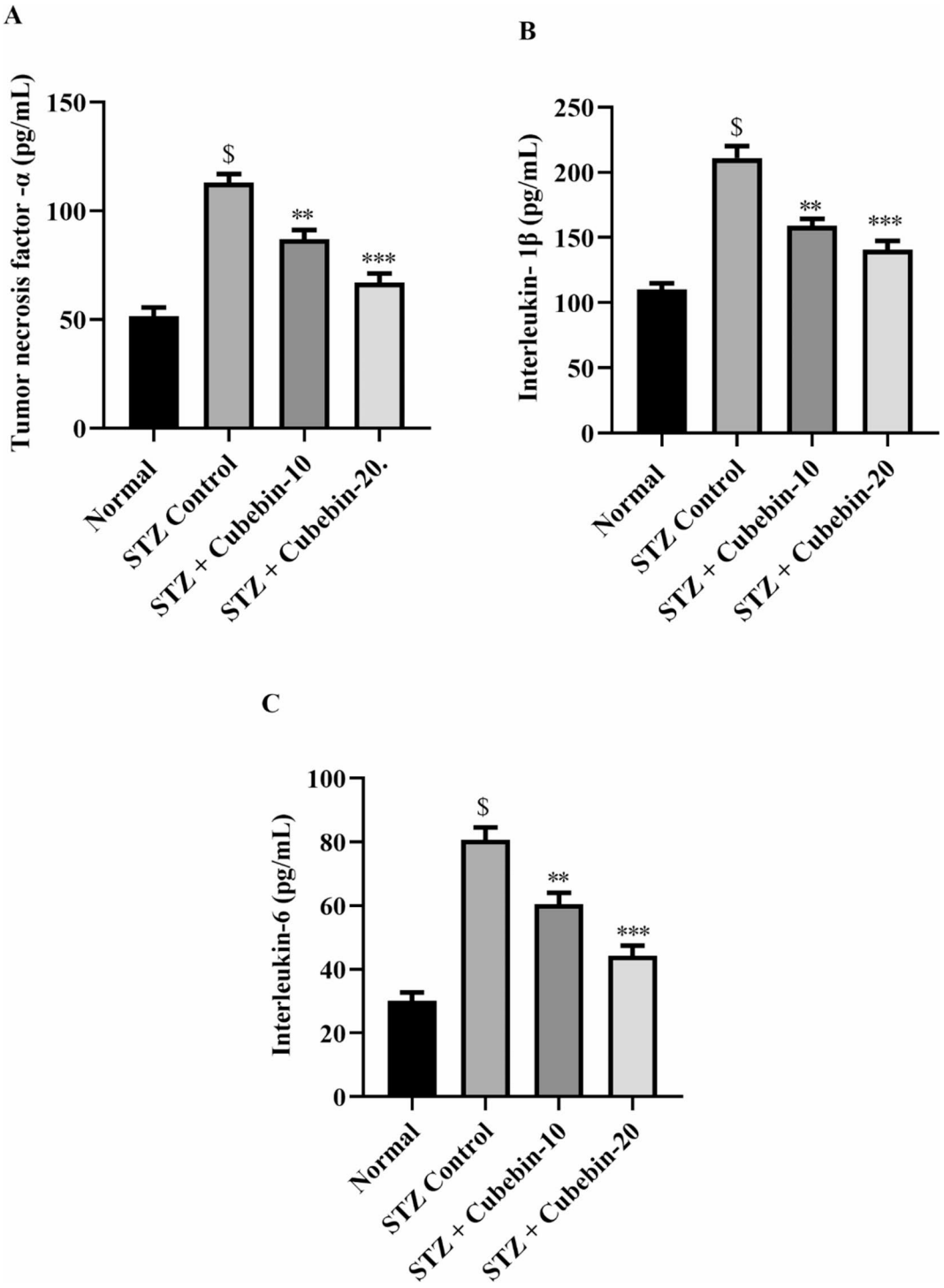

Fig. 7. (**A**–**C**) Cubebin effect on proinflammatory cytokines. (**A**) Tumor necrosis factor-α. (**B**) Interleukin-1β, (**C**) Interleukin-6 (**, ***, $P < 0.001$, $P < 0.0001$; Tukey's test).

exert protective effects against STZ-induced DN. The Ramachandran Plot 7JRA, 1SVC, and 3TZM were retrieved from PROCHECK server and depicted in Fig. 10 and the 3d and 2d images of the interaction of protein TNF-α (PDB ID 7JRA), NF-Kβ (PDB ID 1SVC), TGF-β1 (PDB ID 3TZM) with ligand cubebin depicted in Fig. 11A–C.

Molecular dynamics simulation

MD simulations assessed the conformational stability and convergence of protein-ligand complexes 1SVC, 3TZM, and 7JRA bound to the cubebin ligand. RMSD trajectory served as a metric to quantify the structural fluctuations of the complexes over a 100-nanosecond (ns) simulation. The RMSD plot of 1SVC_cubebin (Fig. 12A) revealed a sharp rise within the initial 10 ns, reaching a maximum value of approximately 3 Å. This

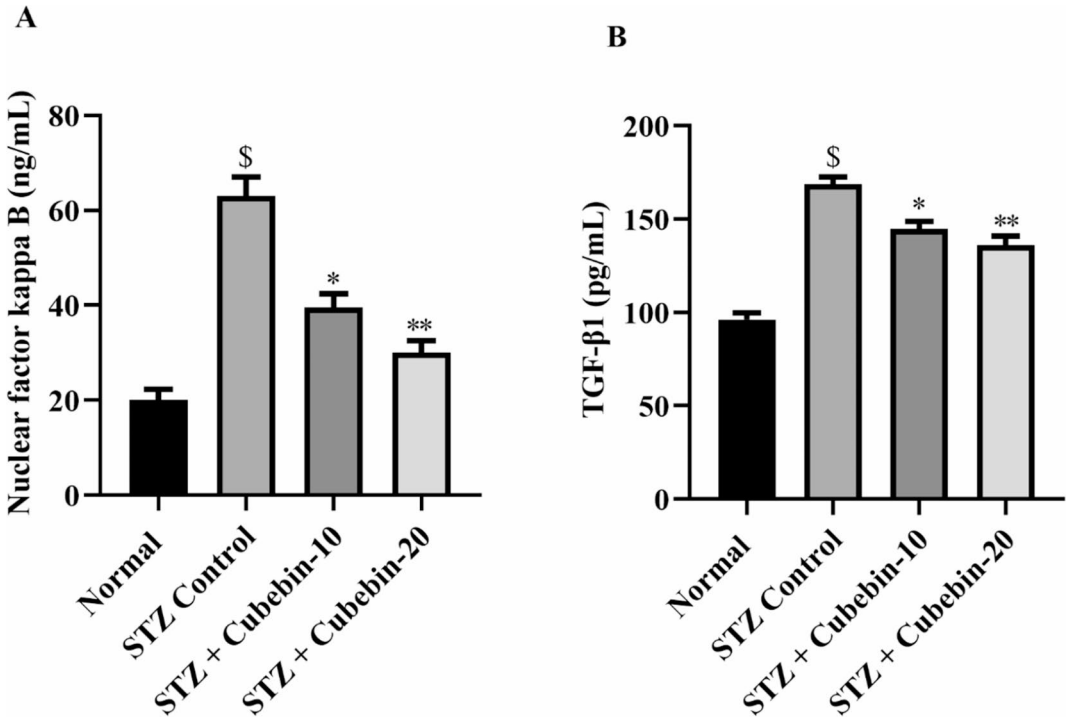

Fig. 8. (**A**,**B**) Cubebin effect on (**A**) Nuclear factor-kappa B and (**B**) Transforming growth factor-β1 (*, **, $P < 0.05$, $P < 0.001$; Tukey's test).

observation suggests significant conformational rearrangements during the system's equilibration phase. The RMSD exhibits periodic fluctuations between 3 Å and 5 Å during the initial phase (10–50 ns), indicative of minor conformational rearrangements within the system while preserving its overall structural integrity. The RMSD values increase from 5 to 6 Å with excursions approaching 7 Å post 50 ns. This leads to the remarkable transition towards a newly formed state of equilibrium around 60 ns maintained with lesser fluctuations.

The RMSD of 4.74 Å was identified for the complex. This stability in the later stages of the simulation suggests the achievement of conformational equilibrium that signifies consistent structural conformation. The RMSD plot for the 3TZM_cubebin complex (Fig. 12B) showed a remarkably lower average RMSD of around 1.36 Å, which indicates higher stability with lesser fluctuations. The initial elevation in RMSD plateaued, leading to an early equilibrium during simulation. The values of RMSD for the 1SVC_cubebin complex showed fluctuations throughout the analysis that highlight the complex with lesser stability compared to 3TZM_cubebin. RMSD plot analysis for the 7JRA_cubebin complex (Fig. 12C) revealed an RMSD of 2.19 Å, suggesting moderate stability with fewer fluctuations than the highly stable 3TZM_cubebin.

Throughout the MD simulation, the RMSF plot visualizes the variations within the 1SVC_cubebin, 3TZM_cubebin, and 7JRA_cubebin complexes. The 1SVC_cubebin complex (Fig. 13A) shows the pronounced peaks around residues 40, 140, 180, and 280, indicating remarkable mobility in these regions with an RMSF value of 5 Å. These values suggest greater conformational freedom for the corresponding residues in the 1SVC_cubebin complex than the other investigated structures. Analysis of RMSF showed elevated values for specific residues that suggest greater conformational flexibility. This enhanced mobility attributes the presence of loops, or solvent-accessible protein surfaces more dynamic. The residues with low RMSF values tend to show stability during the simulation.

The complex shows a higher average RMSF (2.05 Å) than the 3TZM_cubebin complex (0.73 Å), suggesting higher atomic mobility. This flexibility shows the higher RMSD values are less structurally rigid and complex. The average RMSF remains relatively low, which implies the maintenance of overall protein conformation, showing the proper orientation of binding sites for ligand interaction. The 3TZM_cubebin complex shows a different pattern with lower average fluctuations (0.73 Å) and localized peaks reaching a maximum of 3 Å around residues 160 and 220, suggesting a more stable complex with definite regions of flexibility.

The lesser fluctuations among the residue reflect low RMSF values with a greater degree of rigidity and stability that aligns with the findings from the RMSD analysis, indicating high structural strength. The limited flexibility demonstrates the presence of strong interactions among the protein and the cubebin ligand correlating with the low RMSD values, providing evidence for stable and structurally rigid assembly of macromolecules (Fig. 13B).

The RMSF plot of the 7JRA_cubebin complex (Fig. 13C) revealed an intermediate flexibility relative to the other two complexes depicted by the average RMSF values of around 0.91 Å, with peaks reaching up to 6 Å at residues 150 and 300 showing localized regions of high mobility. These outcomes suggest that the 7JRA_cubebin

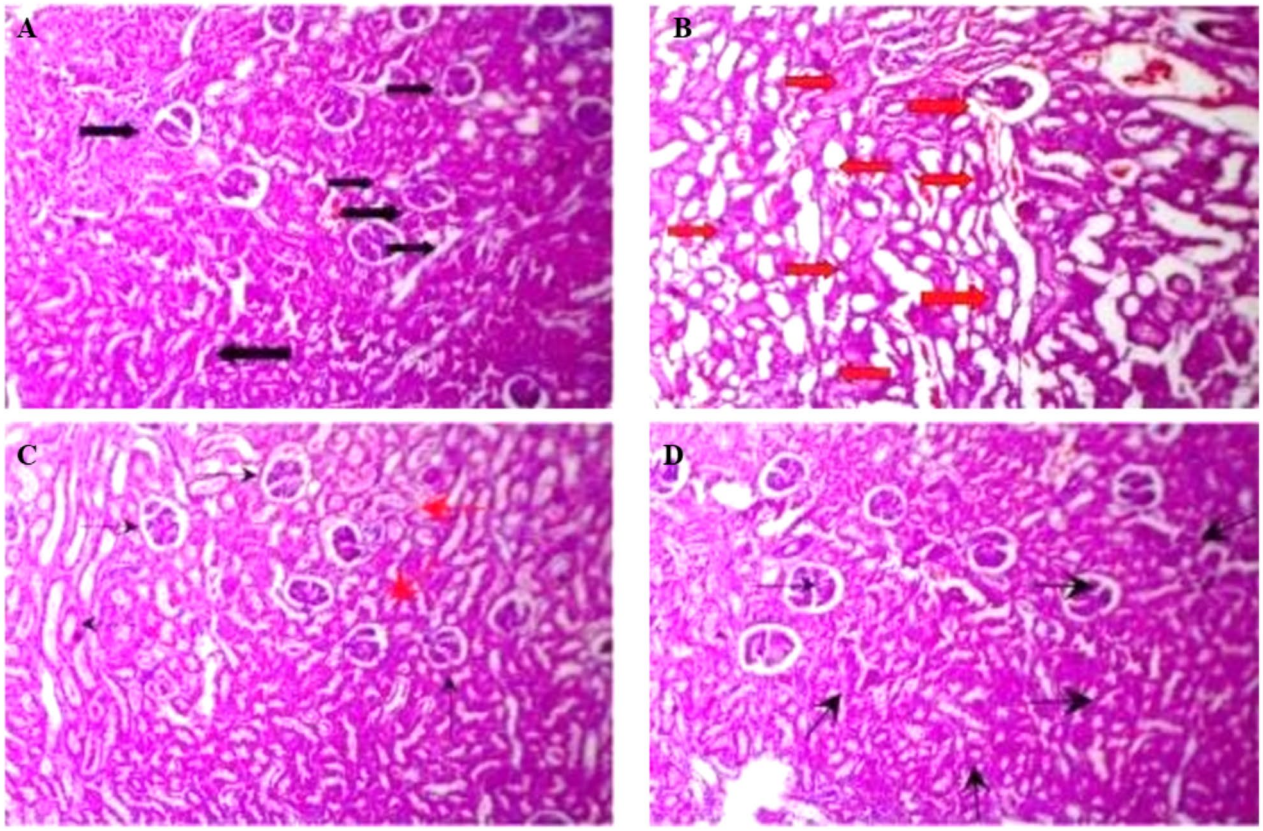

Fig. 9. (**A**–**D**) Histopathology of cubebin on STZ-induced in rat kidney tissue, (**A**) Normal, (**B**) STZ control, red arrow showed cell necrosis and inflammation (**C**,**D**) STZ + cubebin-10- red arrow showed mild inflammation, and black showed mild inhibition of cell necrosis (**D**) STZ + cubebin-20, black arrow showed inhibition of cell necrosis and inflammation.

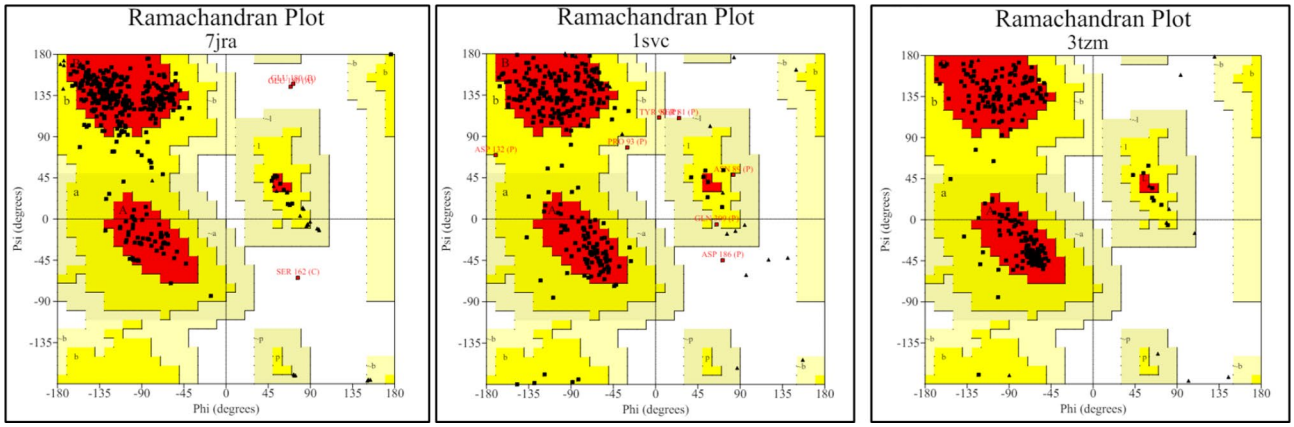

Fig. 10. Ramachandran Plot 7JRA, 1SVC, 3TZM obtained from PROCHECK server.

complex retains the structural integrity accommodating conformational flexibility. Moderate RMSF and RMSD concurrence shows a well-balanced dynamic behaviour inside the complex.

In this study, the Rg plot assessed the behaviour of 1SVC_cubebin, 3TZM_cubebin, and 7JRA_cubebin complexes during a 100 ns molecular dynamics simulation. For the 1SVC_cubebin complex (Fig. 14A), the Rg at 32 Å exhibits a lower within the initial 10 ns that attains stability at 25 Å that signifies a substantial compaction of the protein complex. The fluctuations are observed in Rg values within a range of 32.45–22.03 Å. This observation suggests a stable conformation of the protein complex with minimal variations. The Rg plot (Fig. 14B) shows consistent fluctuations ranging from 26.49 Å to 19.37 Å.

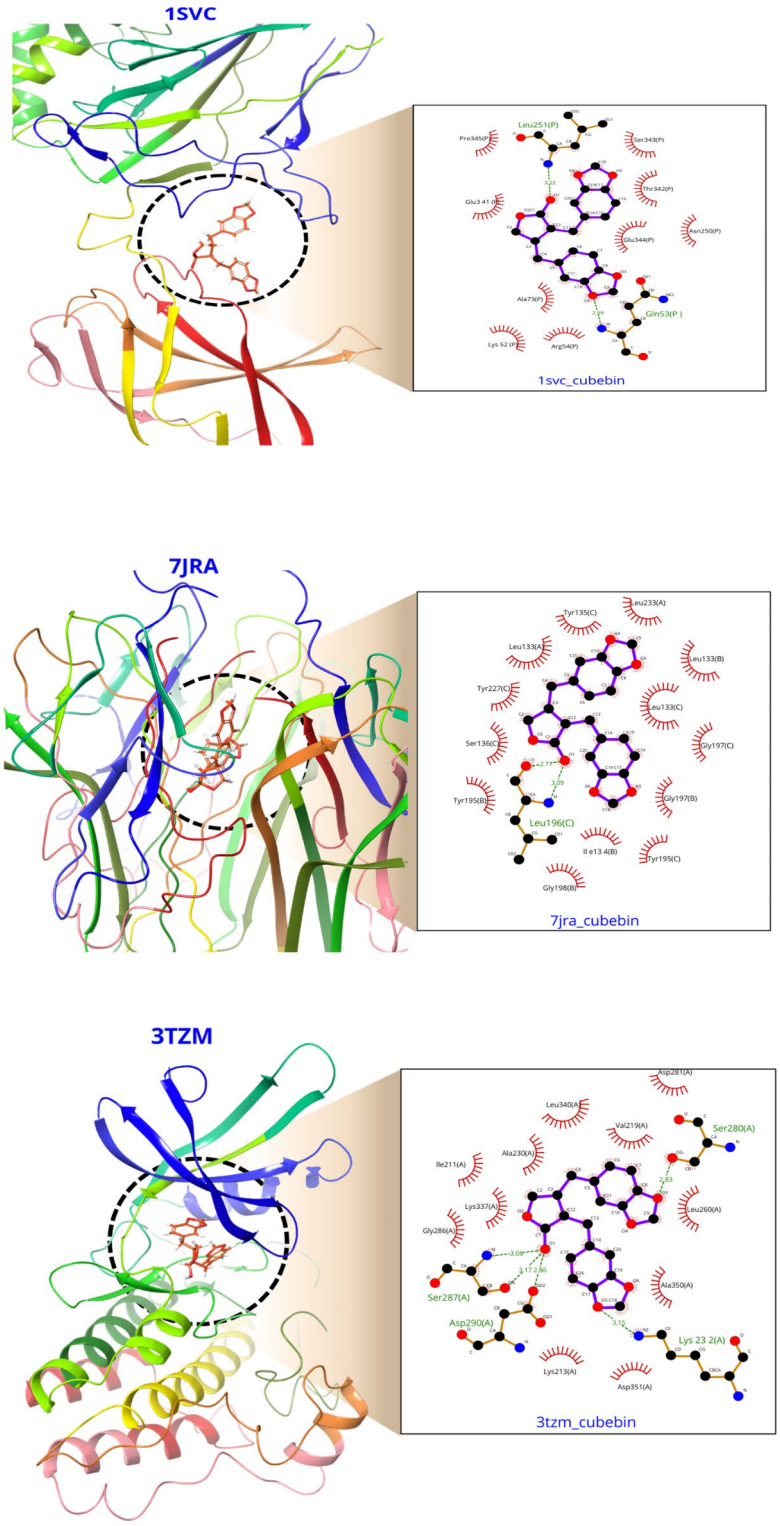

Fig. 11. (**A**–**C**) 3d and 2d images of the interaction of protein TNF-α (PDB ID 7JRA), NF-Kβ (PDB ID 1SVC), TGF-β1 (PDB ID 3TZM) with ligand Cubebin.

The Rg analysis revealed a more dynamic behaviour in the first complex than in the second due to the higher frequency of oscillations, suggesting frequent structural rearrangements. The Rg plot of the second complex (7JRA_cubebin) exhibits significantly less fluctuation, showing a more stable and rigid structure (Fig. 14C). The Rg values range between 21.78 Å and 20.98 Å, reaching a plateau after 10 ns of the simulation. The average Rg value of 21.11 Å further focuses on the compactness and stability of the second complex, which implies minimal conformational changes during the simulation.

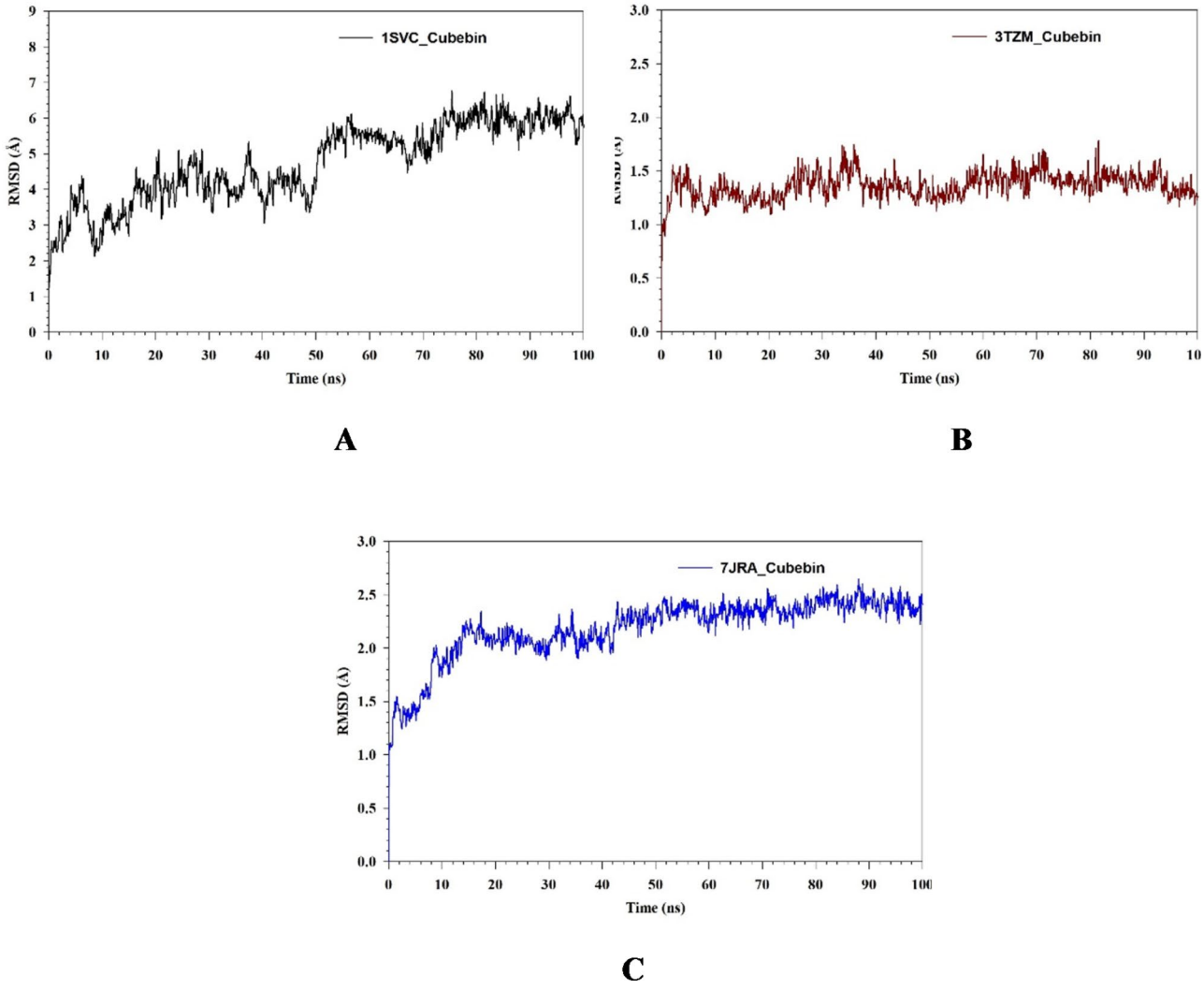

Fig. 12. MD simulation analysis of 100 ns trajectories of (**A**) Cα backbone of RMSD of 1SVC_Cubebin, (**B**) Cα backbone of RMSD of 3TZM_Cubebin, (**C**) Cα backbone of RMSD of 7JRA_Cubebin.

The H-bond plot is responsible for the time-dependent formation of the H-bond within the 1SVC_cubebin, 3TZM_cubebin, and 7JRA_cubebin complexes during a 100 ns molecular dynamics simulation. In the case of 1SVC_cubebin (Fig. 15A), the H-bond number varies between 0 and 4, signifying a continuous process of bond formation and dissociation that underscores the dynamic nature of the protein-ligand interactions. H-bond interactions are used to understand the stability and dynamic behaviour of the complex formed between the 1SVC protein and cubebin. The 1SVC_cubebin complex shows a dynamic H-bond network, with an average of 1.56 bonds, contributing to the complex's flexibility and moderate stability. The H-bond plot for the 3TZM_cubebin complex in Fig. 15B shows more stable interaction, ranging from 0 to 4 bonds. This increased stability in H-bonding relates to RMSD and Rg values observed for the 3TZM_cubebin complex, showing a more rigid and stable structure.

Intermolecular solid interaction between the protein and ligand is observed by the H-bond, which provides the structural integrity of the complex. The 3TZM_cubebin complex has 1.52 H-bonds. These outcomes showed strong intermolecular forces with high stability within the complex structure. Figure 15C represents H-bond interactions in the 7JRA_cubebin complex, which reveals a smaller number of H-bonds that vary from 0 to 3. The absence of an H-bond coincides with the moderate flexibility found in RMSF and Rg values. The limited number of H-bonds suggests weak intermolecular interactions between the ligand and protein that potentially contribute to the moderate stability of the complex.

Analysis of the H-bond revealed that the 7JRA_cubebin complex has fewer interactions with 0.67 bonds, suggesting weaker intermolecular forces and potentially moderating the complex stability. The SASA plot visualizes the solvent exposure of the protein surfaces (1SVC, 3TZM, and 7JRA) in both the unbound (red line) and cubebin-bound (black line) states throughout the simulation. SASA reveals that the 1SVC_cubebin complex exhibits remarkably lower SASA values in the bound state. This observation demonstrates that the binding of cubebin leads to a lowering of the SASA of the protein, indicating a more compact and stable protein-ligand

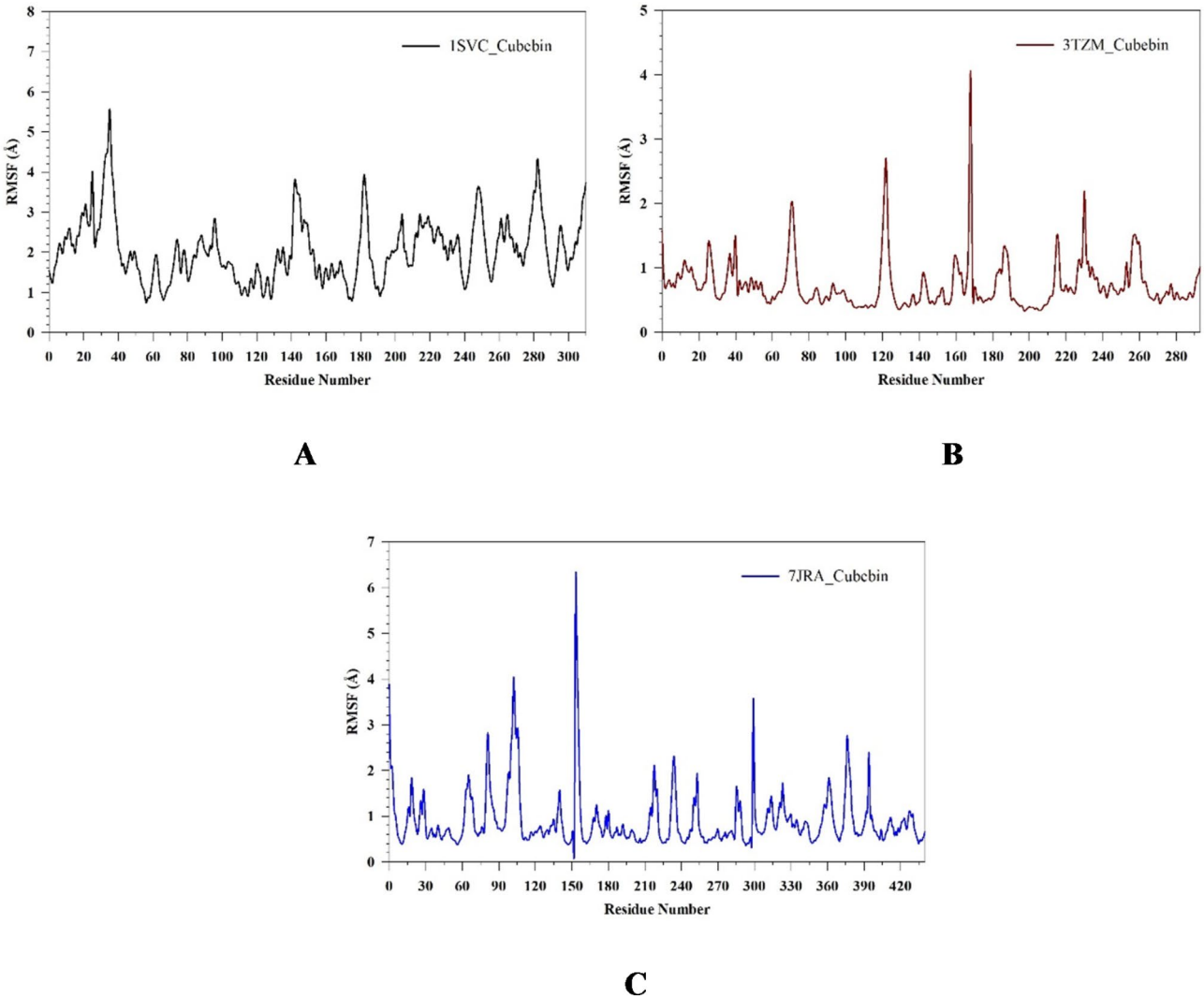

Fig. 13. (**A–C**) MD simulation analysis of 100 ns trajectories of (**A**) RMSF of Cα backbone of 1SVC_Cubebin, (**B**) RMSF of Cα backbone of 3TZM_Cubebin, (**C**) RMSF of Cα backbone of 7JRA_Cubebin.

complex. The decrease in SASA upon ligand binding leads to favourable interactions between cubebin and the protein, where cubebin occludes solvent-accessible regions on the protein's surface. SASA revealed a decline in the accessibility of solvent on ligand binding to the 3TZM protein. The unbound receptor exhibits an average SASA 2.75 times higher than the ligand-bound form. This reduction shows that ligand binding induces a more compact and stable conformation inside the receptor. This supports the decreased solvent exposure observed in the 7JRA_cubebin complex (Fig. 16A-C) and shows the interaction dynamics and stability of protein-ligand complexes that highlight the role of ligand binding in modulating receptor conformation and solvent accessibility.

Figure 17A–C depicts the relative abundance of contact frequency investigated for all the complexes involving cubebin. The analysis showed the ligand interactions within each complex. For the 1SVC_cubebin complex, the ligand established H-bonds with several residues, indicating a strong binding affinity in this region. The residues of LYS52 (34%) and LYS80 (10%) interacted with the ligand by pi-pi stacking. In the 3TZM_cubebin complex, the ligand interacted extensively with ASP351 (84%), LYS232 (86%), and GLU245 (34%) through water bridges that highlight the crucial role of ASP351 (84%) in ligand binding. The H-bond interactions were observed with residues ASP290 (28%), HIS283 (81%), and LYS337 (11%), with the latter residue participating in pi-pi stacking (13%). The 7JRA_cubebin complex exhibited interactions with TYR227 (36%) via water bridges and TYR195 (60%) through H-bond (Fig. 17A–C). These findings collectively elucidate the specific ligand-residue interactions and govern each Cubebin complex's complex formation and stability (Fig. 18A–C).

Molecular mechanics generalized born surface area (MM-GBSA) calculations

In this study, MD simulations combined ΔGbind and its associated energetic components for the 1SVC_cubebin, 3TZM_cubebin, and 7JRA_cubebin complexes using the MM-GBSA method (Table 5). The 1SVC_cubebin complex showed favourable binding affinity, characterized by a ΔGbind of − 50.10 kcal/mol.

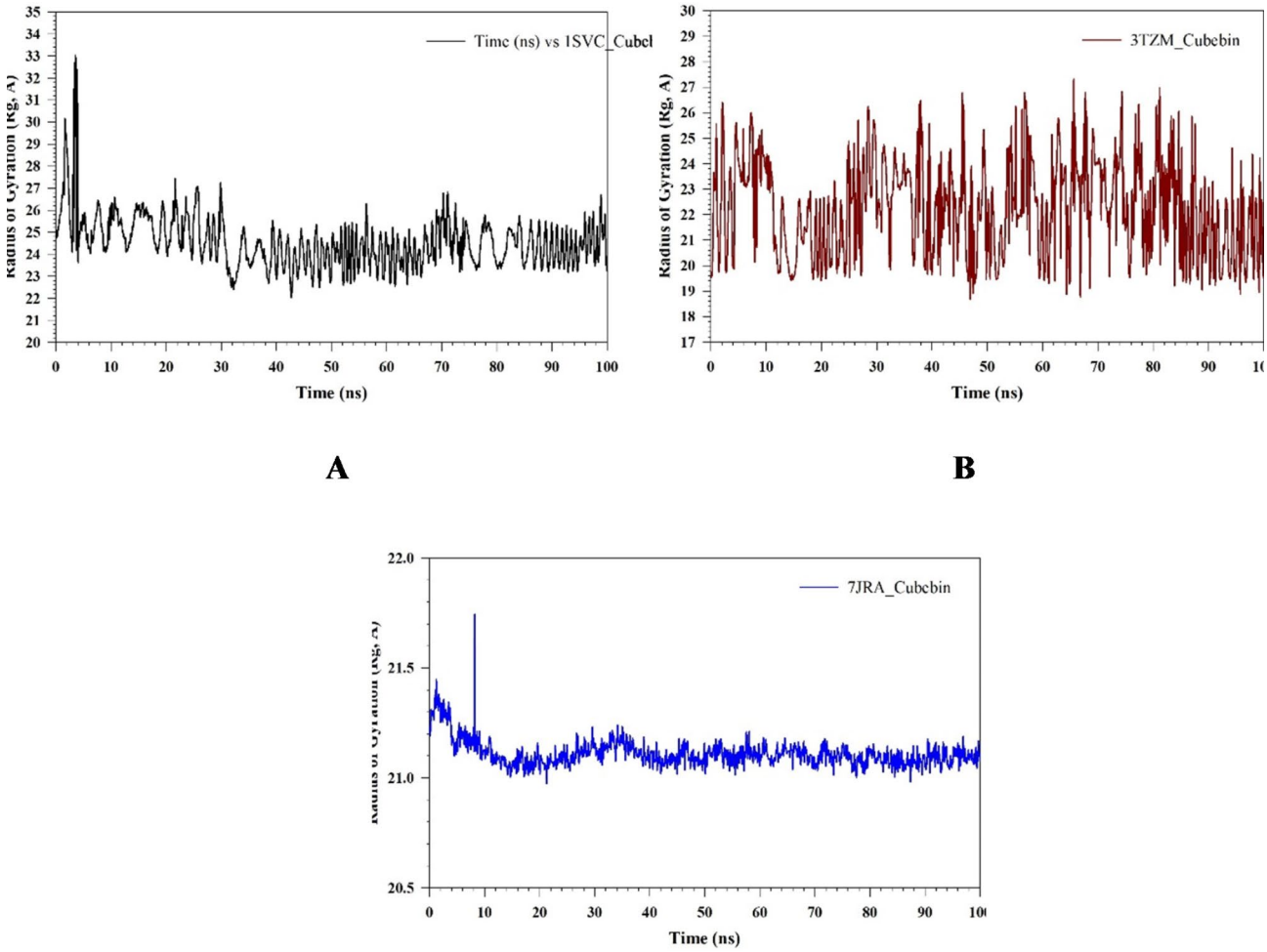

Fig. 14. (**A–C**) MD simulation analysis of 100 ns trajectories of (**A**) Rg of Cα backbone of 1SVC_Cubebin, (**B**) Rg of Cα backbone of 3TZM_Cubebin, (**C**) Rg of Cα backbone of 7JRA_Cubebin.

The overall binding energy profile showed that non-covalent interactions, specifically van der Waals forces, play a significant role in the complex stability. It is supported by the strong binding affinity observed in the 1SVC-cubebin complex attributed to van der Waals and Coulombic interactions. The 3TZM_cubebin complex exhibits a strong binding affinity with a ΔGbind value of -52.84 kcal/mol. The significant contributions to the ΔGbind stem from lipophilic interactions (ΔGbindLipo) and van der Waals forces (ΔGbindvdW) provide the role of hydrophobic contacts in this complex. The contribution of Coulombic interactions is less pronounced compared to the 1SVC_cubebin complex.

The solvation energy (ΔGbindSolvGB) also disfavors binding, although to a lesser extent than the other factors. The 3TZM_cubebin exhibits the strongest binding affinity and is primarily attributed to non-covalent interactions driven by favourable lipophilicity and van der Waals forces. Conversely, the 7JRA_cubebin complex demonstrated the weakest binding affinity, reflected by a ΔGbind value of − 47.75 kcal/mol. Like the other complexes, ΔGbindvdW and ΔGbindLipo remained remarkable contributors to the binding affinity.

However, ΔGbindSolvGB is associated with Complex 7JRA_cubebin, indicating greater energy upon desolvation, contributing to a weaker overall binding affinity. Furthermore, the lower H-bond contribution suggests a lack of specific interactions that stabilize the complexes. The observed higher solvation energy and lower H-bond contribution show that Complex 7JRA_cubebin exhibits a weaker affinity in binding.

Discussion

Type 1 DM is a chronic metabolic disorder that manifests in persistent hyperglycemia due to either a pancreatic deficiency in insulin secretion or a cellular resistance to insulin's action[42,43]. The clinical presentation often includes polydipsia, polyphagia, polyuria, unintended body weight reduction, etc[44]. The modulation of chronic hyperglycemia triggers an upregulation of ROS production in both the mitochondria and cytosol. This resultant oxidative stress is a significant contributor to the development of various diabetic complications. The kidney,

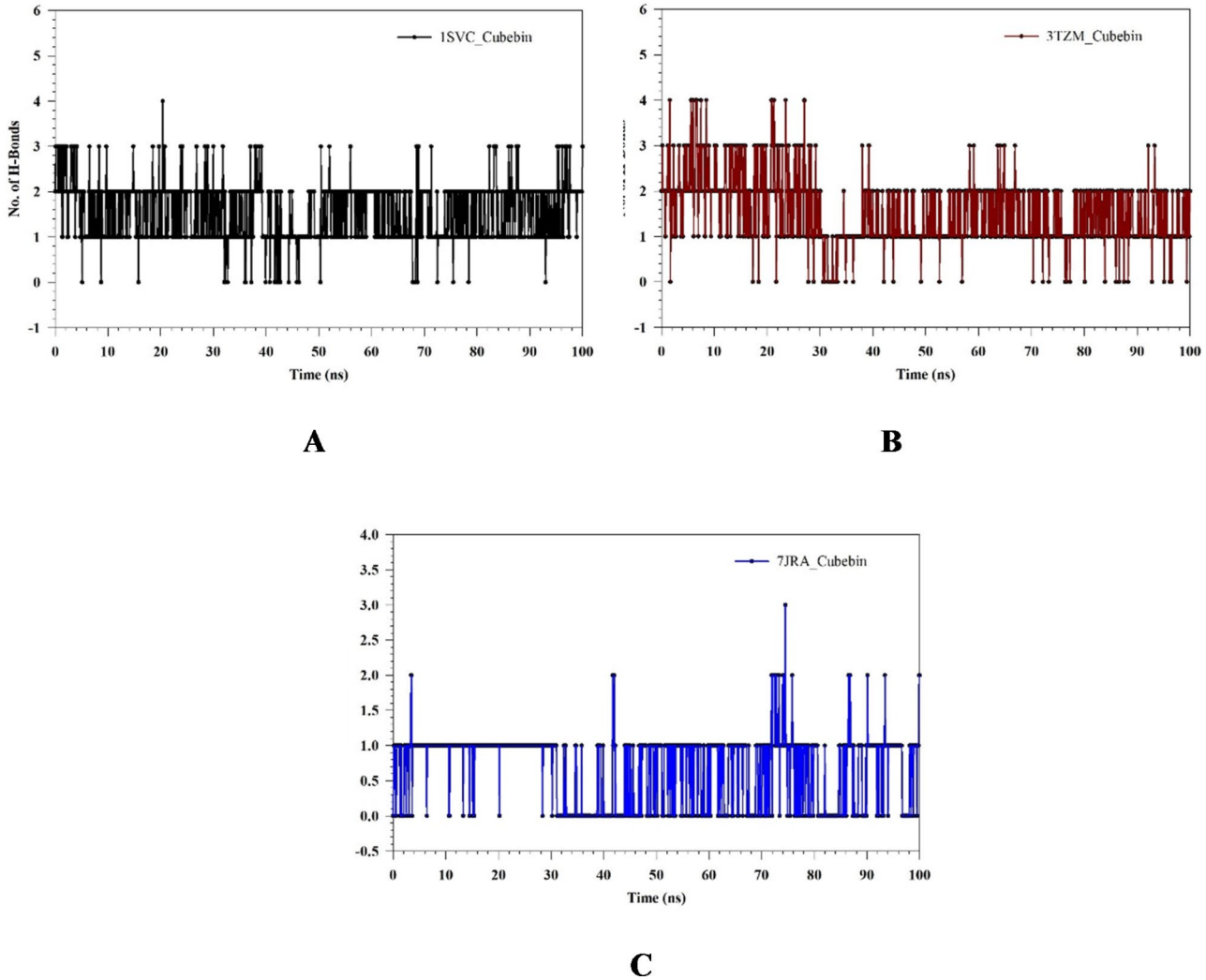

Fig. 15. (**A–C**) MD simulation analysis of 100 ns trajectories of (**A**) Formation of hydrogen bonds in 1SVC_Cubebin, (**B**) Formation of hydrogen bonds in 3TZM_Cubebin, (**C**) Formation of hydrogen bonds in 7JRA_Cubebin.

a highly metabolic organ rich in mitochondria, is particularly susceptible to hyperglycemia-induced oxidative damage. This state is known to exacerbate chronic kidney disease progression[45,46]. Persistent hyperglycemia, a characteristic of DM, has been associated with renal dysfunction, as evidenced by a marked elevation in urea and Scr concentrations observed in the DM[47].

STZ-evoked hyperglycemia represents a well-characterized in vivo model for exploring antidiabetic agents in ameliorating the pathophysiology of diabetes. STZ, a potent diabetogenic agent, is widely utilized to induce experimental type 1 diabetes in animals[48]. STZ exhibits specific, rapid, and irreversible cytotoxic effects on pancreatic β-cells, effectively destroying these insulin-producing cells[49,50].

The proposed study assessed the potential outcome of cubebin in STZ-induced type 1 diabetes and DN in rats. Treatment with cubebin resulted in significant reductions in blood glucose levels, oxidative stress markers, and indicators of renal dysfunction. These findings suggest a protective effect of cubebin against the progression of DN. Previous investigations have consistently shown that hyperglycemia triggers a concomitant rise in blood glucose, oxidative stress markers, and renal function biomarkers, all of which are established hallmarks characterizing the development of DN[26].

STZ serves as a well-established in vivo model for type 1 DM and DN due to its selective induction of necrosis in pancreatic beta-cells, consequently reducing insulin secretion[45]. We observed the administration of STZ, a statistically significant elevation of blood glucose levels within five days. Subsequent intervention with cubebin showed a progressive reduction in blood glucose levels, ultimately achieving normal levels. Therefore, cubebin administration could lower the incidence of kidney dysfunction by suppressing hyperglycemia. Insulin, a polypeptide hormone containing 51 amino acids primarily synthesized by pancreatic β-cells within the islets of Langerhans, exerts significant regulatory influence on glucose homeostasis, cellular growth, and metabolic processes. STZ administration induces partial pancreatic islet dysfunction, initiating an inflammatory cascade that progressively lowers the β-cell activity, leading to insulin deficiency and causing hyperglycemia[22]. We

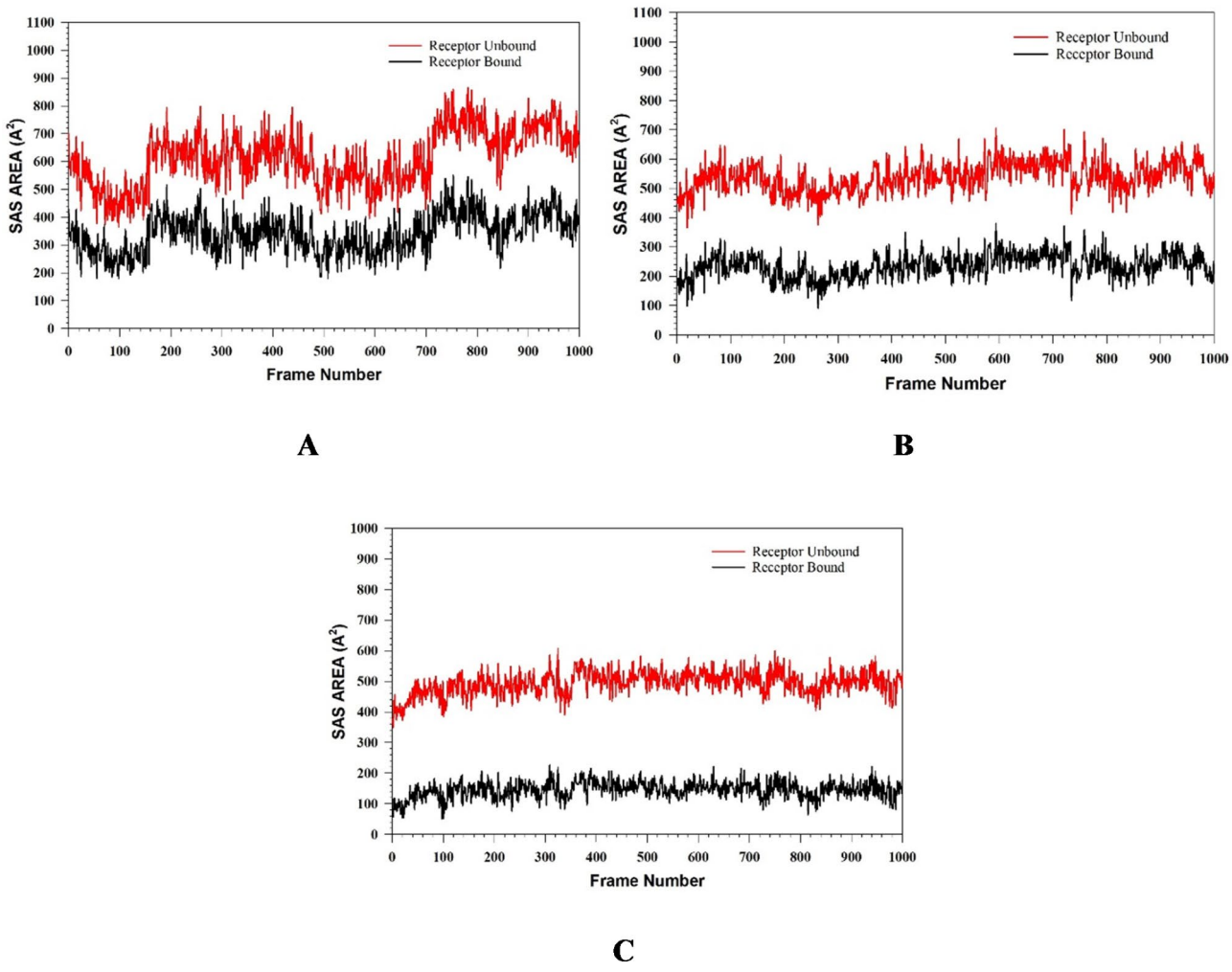

Fig. 16. (**A–C**) MD simulation analysis of 1000 Framework of (**A**) Solvent accessible surface area (SASA) of 1SVC_Cubebin complex. (**B**) The SASA of 3TZM_Cubebin complex. (**C**) The SASA of 7JRA_Cubebin complex.

observed that the administration of STZ caused a reduction in insulin levels while being treated with cubebin, potentially restoring the insulin. HbA1c is a key marker for long-term glycemic regulation, exhibiting the average blood glucose levels. It offers a dependable assessment of chronic hyperglycemia and shows a strong correlation with the potential for developing long-term diabetic complications[51]. Furthermore, elevated HbA1c levels are indirectly associated with an elevated risk of coronary artery disease and stroke, regardless of diabetic status[52]. We observed that the administration of STZ caused an elevation in HbA1c levels while being treated with cubebin, potentially restoring the HbA1c.

Emerging evidence from multiple investigations suggests that hyperglycemia, while a contributing factor, is not solely responsible for the initiation and progression of DM and DN. Recent studies have implicated a cluster of dyslipidemic factors beyond hyperglycemia in disease onset and progression. Recent studies implicate a cluster of lipid abnormalities, including hypertriglyceridemia alongside elevated TC, TG, and LDL-C, and reduced HDL-C, as potential key drivers in the initiation and progression of DM and DN[53,54].

This study demonstrates that STZ administration resulted in elevated cholesterol levels in rats. Notably, treatment with cubebin significantly reduced these levels, suggesting a potential role in regulating lipid metabolism. Furthermore, cubebin treatment significantly restored the imbalance of cholesterol levels, including TC, HDL-C, and TG, observed in STZ-treated rats. This finding suggests that cubebin protects against DN induced by STZ.

Studies have established plasma creatinine as a superior marker for GFR compared to urea. Elevated Scr levels indicate impaired kidney function. Increased BUN, along with Scr, suggests kidney damage or dysfunction. A concurrent rise in urea with blood sugar suggests hyperglycemia-induced kidney injury[55]. DN rats treated with cubebin resulted in a dose-dependent reduction of creatinine, mirroring the observed decrease in urea and BUN levels. These significant reductions in renal and systemic markers of nitrogenous waste products suggest a potential nephroprotective effect of cubebin. They further support the notion that the suppression of renal inflammatory response is responsible for ameliorating the impact of cubebin on renal dysfunction in

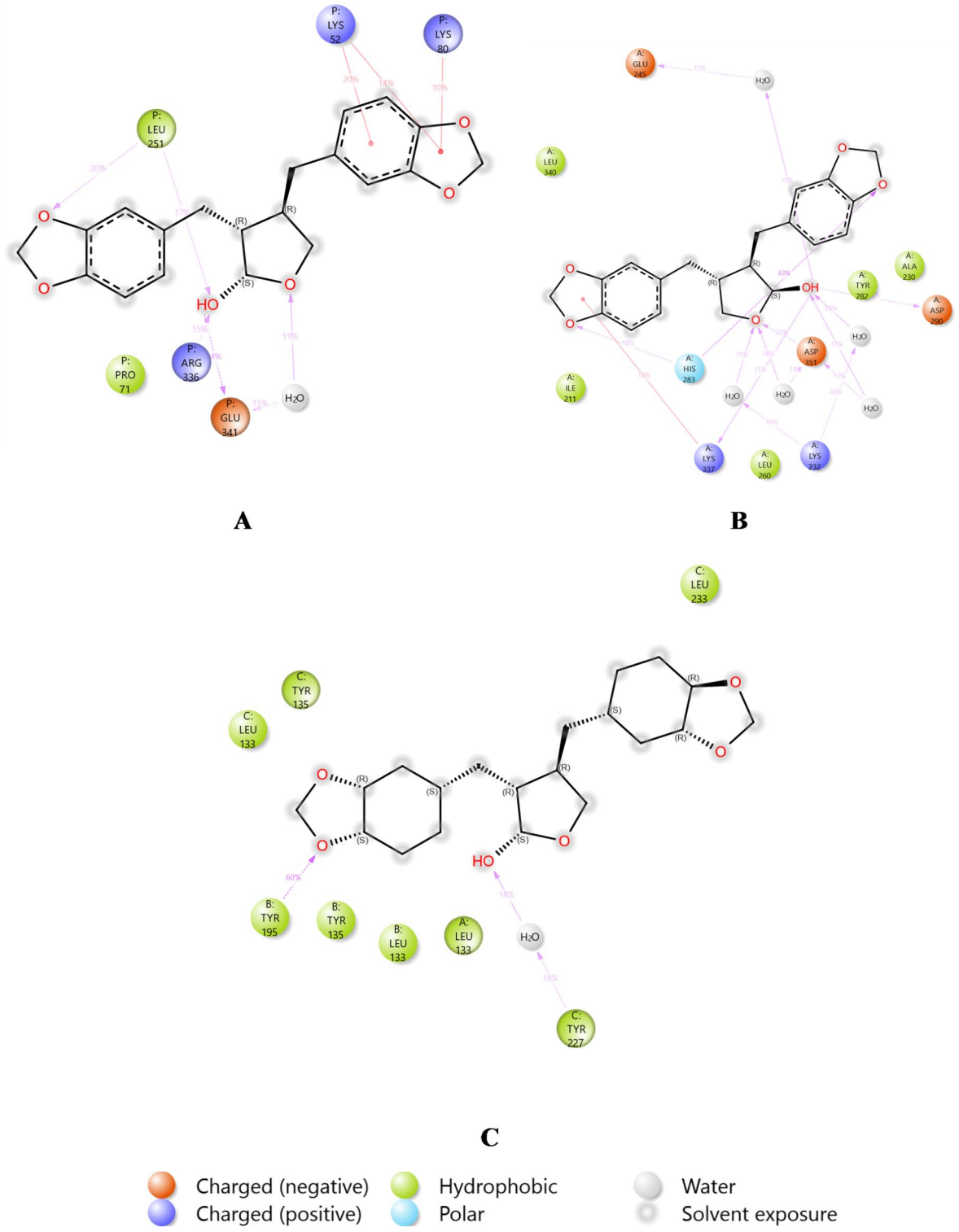

Fig. 17. (**A–C**) Protein-ligand percent interactions of (**A**) 1SVC_Cubebin, (**B**) 3TZM_Cubebin, (**C**) 7JRA_Cubebin.

diabetic rats. These findings further corroborate the hypothesis that the administration of cubebin showed a renoprotective effect in DN rats by attenuating the renal inflammatory response.

A cellular state of oxidative stress ensues when the rate of free radical production surpasses the capacity of the antioxidant defence system. This imbalance leads to the harmful effects of free radicals on cellular constituents. Oxidative stress serves a significant role in diabetic complications through mechanisms including lipid peroxidation, DNA damage, and mitochondrial dysfunction. Additionally, it is implicated in the pathophysiology

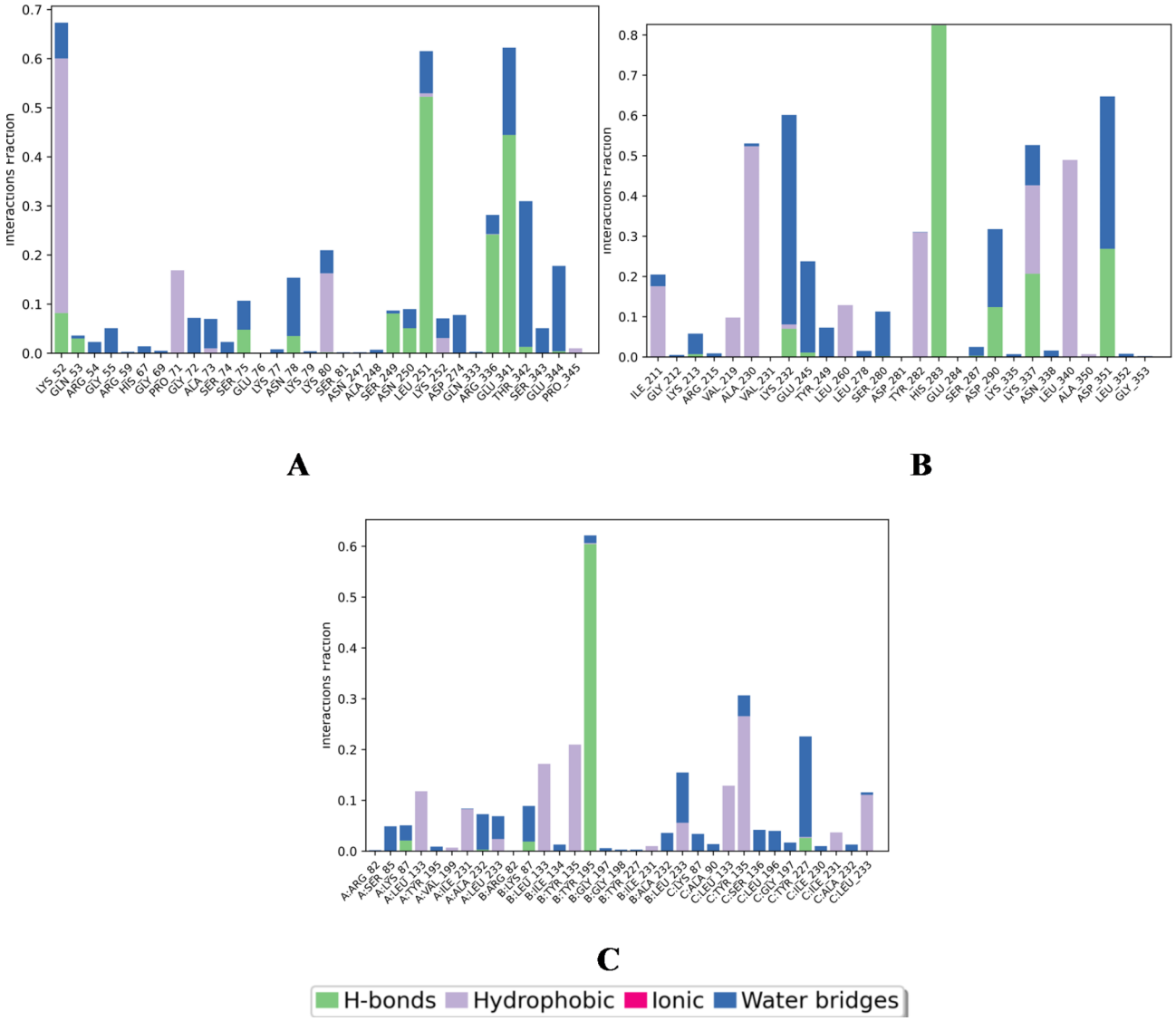

Fig. 18. (**A–C**) Bar graph of Protein-ligand contacts of (**A**) 1SVC_Cubebin, (**B**) 3TZM_Cubebin, (**C**) 7JRA_Cubebin. showing the interaction fraction of amino acid residues over the period of simulation.

of numerous other diseases. Most biological cells have an intrinsic defence mechanism comprising various antioxidant enzymes that safeguard cells from free radical-mediated injury[56]. Our study demonstrated cubebin, a marked enhancement in the activity of antioxidant enzymes, including SOD, GSH, and CAT.

Additionally, a decrease in MDA levels was observed. These findings suggest a potent antioxidant capacity for cubebin. The elevation of SOD, GSH, and CAT signifies its potential for free radical scavenging. At the same time, the reduction in MDA levels indicates the inhibitory effect on lipid peroxidation, a well-established marker of oxidative stress.

Chronic inflammation, as evidenced by various inflammatory markers, has been identified as a key factor influencing DM, encompassing DN's onset and progression. Pro-inflammatory cytokines such as TNF-α, IL-1β, and IL-6, along with chemokines, play a crucial role in insulitis formation. These mediators are released by diabetogenic T-cells and macrophages that initiate inflammatory cascades within pancreatic islets, ultimately leading to β-cell dysfunction and destruction, thus contributing to the pathogenesis of DM and DN[57]. Furthermore, NF-κB, a redox-sensitive transcription factor, regulates inflammatory cytokine production and contributes to the pathogenesis of diabetes. This highlights its dual role in immune response regulation and cytokine expression, potentially influencing the progression of DN[58]. Cubebin administration significantly reduced the TNF-α, IL-1β, IL-6, NF-κB, and TGF-β1 in DN rats. These outcomes corroborate prior studies that reported that the onset of diabetes is accompanied by inflammation[59].

Histopathological examination of rat kidneys following STZ-induced diabetes revealed significant renal dysfunction and structural damage. These findings were characterized by alterations in renal architecture, including tubular necrosis, severe glomerular hypercellularity, intertubular hemorrhage, and inflammatory infiltrates[60]. Renal histopathological alterations observed in DN rats were significantly improved following

treatment with cubebin. Administration of cubebin at doses of 10 and 20 mg/kg to DN rats resulted in a notable restoration of normal renal architecture. This was evidenced by the return of glomeruli and tubules to their typical morphological characteristics. These findings collectively indicate that cubebin treatment exerts a protective effect against the development of renal pathology in DN rats by effectively attenuating the majority of the observed histological lesions.

In silico docking, analysis investigated the potential interaction between cubebin and three target proteins (PDB ID: 7JRA, 1SVC, 3TZM) implicated in various biological processes. The study revealed favourable binding interactions between cubebin and all three targets, with binding affinities of -11.342, -6.665, and − 9.162 kcal/mol. These negative binding affinity scores indicate a thermodynamically favourable interaction, where lower scores represent stronger binding. Among the investigated targets, cubebin exhibited the strongest affinity towards 7JRA. The analysis further suggests that cubebin and the targets likely involve hydrogen bonding and hydrophobic interactions. These interactions are crucial for ligand-protein binding and can significantly influence the binding affinity and specificity. The potential blockade of conserved and functionally critical residues within the active sites of the target proteins by cubebin is an intriguing finding. This blockade could potentially interfere with the normal function of these proteins, leading to downstream biological effects. However, further research is required to assess the specific residues involved in binding and the functional consequences of their inhibition of particular proteins. Based on these outcomes, the docking study demonstrates that treatment with cubebin attributed to protective effects against STZ-induced DN.

The MM/GBSA analysis within the framework of MD simulations was employed to investigate the binding affinities of the cubebin ligand with 1SVC, 3TZM, and 7JRA protein targets[61]. The complex stability throughout the simulation was evaluated through the calculated binding free energies (ΔGbind). The ΔGbind values for 1SVC_cubebin, 3TZM_cubebin, and 7JRA_cubebin complexes were found to be -50.10 ± 3.22 kcal/mol, -52.84 ± 1.57 kcal/mol, and − 47.75 ± 3.45 kcal/mol, respectively. These results suggest that the 3TZM_cubebin complex demonstrated the strongest binding affinity. Conversely, the 7JRA_cubebin complex exhibits the weakest binding affinity among the investigated complexes. The observed low energy states of the complexes during the simulation imply their overall stability, with more negative ΔGbind values signifying greater stability. This study has limitations concerning interpreting and validating the experimental findings due to several relevant considerations. These considerations include small animals, Western blots, histopathology, and immunohistochemistry. This finding suggests that cubebin treatment's hypothetical mechanism of action may be via multifaceted mechanism of action against DN. Cubebin reduced glucose concentration and HbA1c concentration and increased the level of insulin. By scavenging reactive oxygen species and upregulating endogenous antioxidants, it mitigates oxidative stress. Additionally, cubebin's anti-inflammatory properties are evident in its inhibition of pro-inflammatory cytokines like TNF-α, NF-κB, and TGF-β1, thereby alleviating inflammation in the kidney tissue. Treatment with cubebin protects DN patients from developing renal histopathology. Furthermore, Molecular docking and dynamic simulation studies support this mechanism, revealing cubebin's interaction with inflammatory proteins and its potential to induce conformational changes that inhibit their activity. The binding affinity with all three targets: TNF-α, NF-κB, and TGF-β1, with negative binding energies (-11.342 kcal/mol, -6.665 kcal/mol, and − 9.162 kcal/mol, respectively). This indicates that cubebin may potentially interact with all three proteins, suggesting its involvement in modulating their respective pathways. MDS provided insights into the conformational dynamics of TNF-α, NF-κB, and TGF-β1 upon binding to cubebin. These effects of antioxidant, anti-inflammatory, and renal protective actions position cubebin as a promising restorative for the treatment of diabetic nephropathy.

Conclusion

Cubebin maintained blood glucose, oxidative stress markers, lipid profile, and kidney function in STZ-induced DN rats. These findings suggest that cubebin might exert antioxidant and anti-inflammatory effects by suppressing the pro-inflammatory cytokines in the kidney. In silico analysis utilizing molecular docking simulations, they revealed that cubebin potentially modifies the structure of specific target proteins, including TNF-α, NF-κB, and TGF-β1 after binding. These results suggest that the ameliorative effects of cubebin in DN might be due to its antioxidant properties. Further investigation is required to determine cubebin's long-term effects, elucidate the underlying molecular mechanisms in more detail, and compare its efficacy to established DN therapy.

Data availability

All the data of this study is contained in this manuscript. More data related to this study can be accessed upon a reasonable request to the corresponding author or ru.syed@outlook.com.

Received: 24 October 2024; Accepted: 17 January 2025
Published online: 05 February 2025

References

1. Kumari, S. et al. Nephroprotective effect of Vanillic acid in STZ-induced diabetic rats. *J. Diabetes Metab. Disord.* **20** (1), 571–582 (2021).
2. Diagnosis and classification of diabetes: standards of Care in Diabetes—2024. *Diabetes Care*, **47**(Supplement_1), S20–S42 (2024).
3. Hussain, M. S. et al. Long-term use of metformin and vitamin B12 Deficiency in Diabetes. *Curr. Drug Saf.* 20 (2024).
4. Banday, M. Z., Sameer, A. S. & Nissar, S. Pathophysiology of diabetes: an overview. *Avicenna J. Med.* **10** (04), 174–188 (2020).
5. Seedevi, P. et al. Anti-diabetic activity of crude polysaccharide and rhamnose-enriched polysaccharide from G. lithophila on Streptozotocin (STZ)-induced in Wistar rats. *Sci. Rep.* **10** (1), 556 (2020).

6. Bahl, G. et al. Persistent chronic calcific pancreatitis with intraductal calculi associated with secondary diabetes mellitus type 3 and diabetic ketoacidosis - a case report. *Endocr. Regul.* **58** (1), 101–104 (2024).
7. Guo, L. et al. Nephroprotective Effect of Adropinin Against Streptozotocin-Induced Diabetic Nephropathy in rats: inflammatory mechanism and YAP/TAZ factor. *Drug Des. Devel Ther.* **15**, 589–600 (2021).
8. Hussain, M. S. et al. Therapeutic landscape of diabetic nephropathy: insights from long noncoding RNAs. *Clin. Diabetol.* **13** (5), 307–318 (2024).
9. Samsu, N. Diabetic Nephropathy: challenges in Pathogenesis, diagnosis, and treatment. *Biomed. Res. Int.* **2021**, p1497449 (2021).
10. Saeedi, P. et al. Global and regional diabetes prevalence estimates for 2019 and projections for 2030 and 2045: results from the International Diabetes Federation Diabetes Atlas, 9(th) edition. *Diabetes Res. Clin. Pract.* **157**, p107843 (2019).
11. Rao, V. et al. *Diabetic Nephropathy: An Update on Pathogenesis and drug Development*13p. 754–762 (Clinical Research & Reviews, 2019).
12. Dai, B. et al. The effect of Liuwei Dihuang decoction on PI3K/Akt signaling pathway in liver of type 2 diabetes mellitus (T2DM) rats with insulin resistance. *J. Ethnopharmacol.* **192**, 382–389 (2016).
13. Chen, N. et al. Effect of miR-1297 on kidney Injury in rats with Diabetic Nephropathy through the PTEN/PI3K/AKT pathway. *Arch. Esp. Urol.* **77** (2), 183–192 (2024).
14. Guo, L. et al. *Nephroprotective Effect of Adropinin against streptozotocin-induced Diabetic Nephropathy in rats: Inflammatory Mechanism and YAP/TAZ Factor*, pp. 589–600 (Drug Design, Development and Therapy, 2021).
15. Li, W. et al. The signaling pathways of selected traditional Chinese medicine prescriptions and their metabolites in the treatment of diabetic cardiomyopathy: a review. *Front. Pharmacol.* **15**, 1416403 (2024).
16. Umanath, K. & Lewis, J. B. Update on diabetic nephropathy: core curriculum 2018. *Am. J. Kidney Dis.* **71** (6), 884–895 (2018).
17. Agarwal, R. *Pathogenesis of diabetic nephropathy.* (2021).
18. Cheng, X. et al. Quercetin: a promising therapy for diabetic encephalopathy through inhibition of hippocampal ferroptosis. *Phytomedicine* **126**, 154887 (2024).
19. Herrera, G. A. et al. *Pathogenesis: Structural Changes in the Kidneys in Type 1 and Type 2 Diabetes*, pp. 105–154 (Diabetes and Kidney Disease, 2022).
20. Haghani, F. et al. Aloe vera and Streptozotocin-induced diabetes mellitus. *Revista Brasileira De Farmacognosia*. **32** (2), 174–187 (2022).
21. Akinlade, O. M., Owoyele, B. V. & Soladoye, A. O. Streptozotocin-induced type 1 and 2 diabetes in rodents: a model for studying diabetic cardiac autonomic neuropathy. *Afr. Health Sci.* **21** (2), 719–727 (2021).
22. Furman, B. L. Streptozotocin-induced diabetic models in mice and rats. *Curr. Protocols*. **1** (4), e78 (2021).
23. Li, H. et al. The effects of Warfarin on the pharmacokinetics of Senkyunolide I in a rat model of biliary drainage after administration of Chuanxiong. *Front. Pharmacol.* **9**, 1461 (2018).
24. Zeng, Y. F. et al. Preclinical evidence of reno-protective effect of quercetin on acute kidney injury: a meta-analysis of animal studies. *Front. Pharmacol.* **14**, 1310023 (2023).
25. Behl, T. et al. Alkaloidal phytoconstituents for diabetes management: exploring the unrevealed potential. *Molecules* **27** (18), 5851 (2022).
26. Kumari, S. et al. Nephroprotective effect of Vanillic acid in STZ-induced diabetic rats. *J. Diabetes Metabolic Disorders*. **20**, 571–582 (2021).
27. Borges, A. et al. Molecular interaction analysis of the lignans from Piper cubeba in complex with Haemonchus Contortus phosphomethyltransferase. *Vet. Parasitol.* **321**, 110001 (2023).
28. Bastos, J. K. et al. Anti-inflammatory activity of cubebin, a lignan from the leaves of Zanthoxyllum Naranjillo Griseb. *J. Ethnopharmacol.* **75** (2–3), 279–282 (2001).
29. Souza, G. H. B. et al. Analgesic and anti-inflammatory activities evaluation of (-)-O-acetyl,(-)-O-methyl,(-)-O-dimethylethylamine cubebin and their preparation from (-)-cubebin. *Il Farmaco*. **59** (1), 55–61 (2004).
30. Maistro, E. L. et al. Genotoxic effects of (–)-cubebin in somatic cells of mice. *J. Appl. Toxicol.* **31** (2), 185–189 (2011).
31. Pires, D. E. V., Blundell, T. L. & Ascher, D. B. pkCSM: Predicting Small-Molecule Pharmacokinetic and Toxicity properties using graph-based signatures. *J. Med. Chem.* **58** (9), 4066–4072 (2015).
32. ALTamimi, J. Z. et al. Ellagic acid protects against diabetic nephropathy in rats by regulating the transcription and activity of Nrf2. *J. Funct. Foods.* **79**, 104397 (2021).
33. Tang, L. et al. Quercetin liposomes ameliorate streptozotocin-induced diabetic nephropathy in diabetic rats. *Sci. Rep.* **10** (1), 2440 (2020).
34. Bowers, K. J. et al. Scalable algorithms for molecular dynamics simulations on commodity clusters. In *Proceedings of the ACM/IEEE Conference on Supercomputing*. (2006).
35. Chow, E. et al. *Desmond performance on a cluster of multicore processors.* DE Shaw Research Technical Report DESRES/TR–2008-01, (2008).
36. Shivakumar, D. et al. Prediction of absolute solvation free energies using molecular dynamics free energy perturbation and the OPLS force field. *J. Chem. Theory Comput.* **6** (5), 1509–1519 (2010).
37. Jorgensen, W. L. et al. Comparison of simple potential functions for simulating liquid water. *J. Chem. Phys.* **79** (2), 926–935 (1983).
38. Martyna, G. J., Tobias, D. J. & Klein, M. L. Constant pressure molecular dynamics algorithms. *J. Chem. Phys.* **101** (5), 4177–4189 (1994).
39. Toukmaji, A. Y. & Board, J. A. Jr Ewald summation techniques in perspective: a survey. *Comput. Phys. Commun.* **95** (2–3), 73–92 (1996).
40. Kagami, L. P. et al. Geo-Measures: a PyMOL plugin for protein structure ensembles analysis. *Comput. Biol. Chem.* **87**, 107322 (2020).
41. Bosshard, H. R., Marti, D. N. & Jelesarov, I. Protein stabilization by salt bridges: concepts, experimental approaches and clarification of some misunderstandings. *J. Mol. Recognit.* **17** (1), 1–16 (2004).
42. Hussain, M. S. & Sharma, G. The Burden of Cardiovascular diseases due to COVID-19 pandemic. *Thorac. Cardiovasc. Surg.* **72** (1), 40–50 (2024).
43. Li, X. et al. Screening for primary aldosteronism on and off interfering medications. *Endocrine* **83** (1), 178–187 (2024).
44. Xu, T. et al. Revealing the improvement of diabetes by Si Wei Jiang Huang Tang San through ERK/HIF1α signaling pathway via network pharmacology. *J. Ethnopharmacol.* **319**, 117254 (2024).
45. González, P. et al. Hyperglycemia and oxidative stress: an integral, updated and critical overview of their metabolic interconnections. *Int. J. Mol. Sci.* **24** (11), 9352 (2023).
46. Chen, Y. et al. Catalpol ameliorates fructose-induced renal inflammation by inhibiting TLR4/MyD88 signaling and uric acid reabsorption. *Eur. J. Pharmacol.* **967**, 176356 (2024).
47. Wu, T. et al. The mechanism of hyperglycemia-induced renal cell injury in diabetic nephropathy disease: an update. *Life* **13** (2), 539 (2023).
48. Ghasemi, A. & Jeddi, S. Streptozotocin as a tool for induction of rat models of diabetes: a practical guide. *Excli J.* **22**, 274 (2023).
49. Ghasemi, A. & Jeddi, S. Streptozotocin as a tool for induction of rat models of diabetes: a practical guide. *Excli J.* **22**, 274–294 (2023).
50. Gao, X. H. et al. Structure-activity study of fluorine or chlorine-substituted cinnamic acid derivatives with tertiary amine side chain in acetylcholinesterase and butyrylcholinesterase inhibition. *Drug Dev. Res.* **80** (4), 438–445 (2019).

51. Lu, Q. Q. et al. Nitrogen-containing flavonoid and their analogs with diverse B-ring in acetylcholinesterase and butyrylcholinesterase inhibition. *Drug Dev. Res.* **81** (8), 1037–1047 (2020).
52. Casadei, G., Filippini, M. & Brognara, L. Glycated hemoglobin (HbA1c) as a biomarker for diabetic foot peripheral neuropathy. *Diseases* **9** (1), 16 (2021).
53. Alatawi, K. A. & Alshubaily, F. A. Coconut products alleviate hyperglycaemic, hyperlipidimic and nephropathy indices in streptozotocin-induced diabetic wistar rats. *Saudi J. Biol. Sci.* **28** (8), 4224–4231 (2021).
54. Feingold, K. R. & Grunfeld, C. Diabetes and dyslipidemia, in Diabetes and Cardiovascular Disease. 425–472 (Springer, 2023).
55. Hassanalilou, T. et al. The protective effects of Morus nigra L. leaves on the kidney function tests and kidney and liver histological structures in streptozotocin-induced diabetic rats. *Biomed. Res.* **28** (14), 6113–6118 (2017).
56. Yaribeygi, H. et al. *Molecular mechanisms linking oxidative stress and diabetes mellitus.* Oxidative medicine and cellular longevity, 2020. (2020).
57. Donate-Correa, J. et al. Inflammatory cytokines in diabetic kidney disease: pathophysiologic and therapeutic implications. *Front. Med.* **7**, 628289 (2021).
58. Amirshahrokhi, K. & Zohouri, A. Carvedilol prevents pancreatic β-cell damage and the development of type 1 diabetes in mice by the inhibition of proinflammatory cytokines, NF-κB, COX-2, iNOS and oxidative stress. *Cytokine* **138**, 155394 (2021).
59. Gilani, S. J. et al. Rosinidin flavonoid ameliorates hyperglycemia, lipid pathways and proinflammatory cytokines in streptozotocin-induced diabetic rats. *Pharmaceutics* **14** (3), 547 (2022).
60. Rahmani, A. H. et al. Quercetin, a plant flavonol attenuates diabetic complications, renal tissue damage, renal oxidative stress and inflammation in streptozotocin-induced diabetic rats. *Metabolites* **13** (1), 130 (2023).
61. Kazmi, I. et al. Influence of rosiridin on streptozotocin-induced diabetes in rodents through endogenous antioxidants-inflammatory cytokines pathway and molecular docking study. *J. Biomol. Struct. Dynamics* 1–16 (2023).

Acknowledgements

This research has been funded by Deputy for Research and Innovation, Ministry of Education through Initative of Institutional Funding at University of Ha'il-Saudi Arabia through project number IFP-22 191.

Author contributions

Rahamat Unissa Syed: Writing – review & editing, Writing – original draft, Investigation, Data curation, Conceptualization. Sivakumar S. Moni: Writing – original draft, Investigation, Data curation. Weiam Hussein: Writing – original draft, Investigation, Data curation. Taghreed Mohammad Saad Alhaidan: Visualization. Sondos Mohammed Y Abumi: Writing – review & editing, Visualization, Supervision, Resources. Lama Khalid Alnahdi: Writing – original draft, Investigation, Data curation. Ling Shing Wong, Vetriselvan Subramaniyan and Vinoth Kumarasamy: Writing – original draft, Investigation, Data Curation.

Declarations

Competing interests

The authors declare no competing interests.

Additional information

Correspondence and requests for materials should be addressed to R.U.S., S.S.M. or V.K.